The Observed North Equatorial Countercurrent in the Far Western Pacific Ocean during the 2014–16 El Niño

HUI ZHOU,[a,b] HENGCHANG LIU,[a,b] SHUWEN TAN,[a,b] WENLONG YANG,[a,b] YAO LI,[a] XUEQI LIU,[a,b]
QIANG REN,[a] AND WILLIAM K. DEWAR[c,d]

[a] CAS Key Laboratory of Ocean Circulation and Waves, Institute of Oceanology, Chinese Academy of Sciences, and Pilot National
Laboratory for Marine Science and Technology (Qingdao), Qingdao, China
[b] University of Chinese Academy of Sciences, Beijing, China
[c] Department of Ocean, Atmosphere and Earth Sciences, The Florida State University, Tallahassee, Florida
[d] Université Grenoble Alpes, CNRS, IRD, Grenoble INP, IGE, Grenoble, France

ABSTRACT: The structure and variations of the North Equatorial Countercurrent (NECC) in the far western Pacific Ocean during 2014–16 are investigated using repeated in situ hydrographic data, altimeter data, Argo data, and reanalysis data. The NECC shifted ~1° southward and intensified significantly with its transport exceeding 40 Sv (1 Sv ≡ 10^6 m^3 s^{-1}), nearly double its climatology value, during the developing phase of the 2015/16 El Niño event. Observations show that the 2015/16 El Niño exerted a comparable impact on the NECC with that of the extreme 1997/98 El Niño in the far western Pacific Ocean. Baroclinic instability provided the primary energy source for the eddy kinetic energy (EKE) in the 2015/16 El Niño, which differs from the traditional understanding of the energy source of EKE as barotropic instability in low-latitude ocean. The enhanced vertical shear and the reduced density jump between the NECC layer and the North Equatorial Subsurface Current (NESC) layer renders the NECC–NESC system baroclinically unstable in the western Pacific Ocean during El Niño developing phase. The eddy–mean flow interactions here are diverse associated with various states of El Niño–Southern Oscillation (ENSO).

KEYWORDS: Baroclinic flows; El Nino; ENSO; Instability; Ocean circulation; Ocean dynamics

1. Introduction

The western equatorial Pacific Ocean plays an important role in the initiation of El Niño–Southern Oscillation (ENSO) due to its active air–sea interactions (Wyrtki 1975, 1985; Weisberg and Wang 1997; Wang et al. 1999; Kessler et al. 2003). This region is also the source region of the Pacific-to-Indian Ocean Throughflow (Gordon and Fine 1996; Fieux et al. 1994), which is an important part of the so-called great conveyor belt (Gordon 1986). Therefore, understanding the structure and variability of the ocean circulation here are key factors in the study of ENSO and global climate changes.

The surface current system here (Fig. 1a) contains the North Equatorial Current (NEC), which bifurcates into two western boundary currents at the Philippine coast (Schott 1939; Nitani 1972; Toole et al. 1990). The southward western boundary current is named as the Mindanao Current (MC), which flows along the east coast of Mindanao Island, and it counters the New Guinea Coastal Current/Undercurrent (NGCC/NGCUC)

near the entrance of the Celebes Sea. These flows retroflect to the east and form the source of the North Equatorial Countercurrent (NECC), hence the nascent NECC, which exhibits a large meander accompanied by two semipermanent eddies: the cyclonic Mindanao Eddy (ME) centered around 7°N, 128°E and the anticyclonic Halmahera Eddy (HE) centered around 3°–4°N, 131°E (Wyrtki 1961; Masumoto and Yamagata 1991; Qiu and Lukas 1996; Heron et al. 2006; Zhou et al. 2010; Kashino et al. 2013).

On average, the NECC transports about 10–30 Sv (1 Sv ≡ 10^6 m^3 s^{-1}) of the convergent surface water from the warm pool in the western Pacific to the eastern tropical Pacific Ocean (Wyrtki and Kendall 1967; Johnson et al. 2002). Its interannual variations have been proposed to be closely connected to ENSO with strong transport and southward shift of its axis during El Niño events (Wyrtki 1979; Meyers and Donguy 1984; Kessler and Taft 1987; Taft and Kessler 1991; Delcroix et al. 1992; Qiu and Joyce 1992; Johnson et al. 2002; Kessler 2006; Hsin and Qiu 2012; Zhao et al. 2013; Chen et al. 2016; Tan and Zhou 2018, hereafter TZ18). The NECC plays a key role in shaping the tropical Pacific climate, such as the equatorial asymmetry of the intertropical convergence zone (ITCZ; Richards et al. 2009; Masunaga and L'Ecuyer 2011), and modulates the warm pool heat budget through the displacement of the western Pacific warm pool in the east–west direction (Meyers and Donguy 1984; Picaut and Delcroix 1995; Kessler et al. 2003; Clement et al. 2005). Therefore, details of the NECC structure and variability are required for a better understanding of the ENSO and climate variability in the tropical Pacific region.

ⓐ Denotes content that is immediately available upon publication as open access.

🖉 Supplemental information related to this paper is available at the Journals Online website: https://doi.org/10.1175/JPO-D-20-0293.s1.

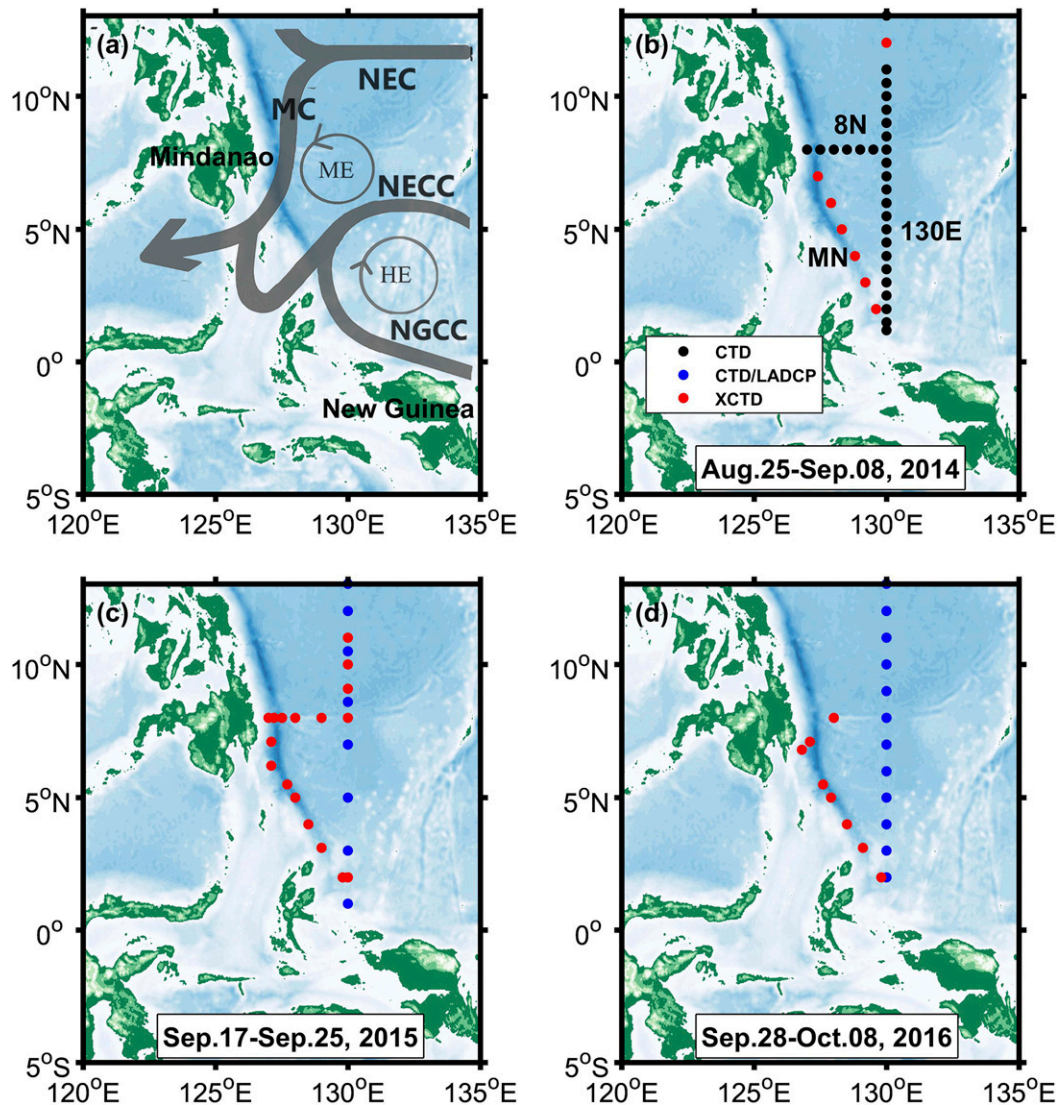*Corresponding author*: Hui Zhou, zhouhui@qdio.ac.cn

FIG. 1. (a) A schematic of the surface current system and observation stations during (b) 2014, (c) 2015, and (d) 2016 cruises by the R/V *Kexue* in the far western Pacific Ocean. In (b), 8N and 130E represent the zonal and meridional transect at 8°N and 130°E, respectively. MN represents the transect between Mindanao Island and New Guinea Island. The date for each cruise is labeled in the bottom.

Although some observations have been conducted on the NECC in the Pacific Ocean, most of them focus on the NECC east of 140°E (Wyrtki and Kendall 1967; Delcroix et al. 1987, 1992; Philander et al. 1987; Johnson et al. 2002; Brown et al. 2007; Richards et al. 2009; Sprintall et al. 2009; Wang et al. 2016). By contrast, observations in the birthplace of the NECC are quite few (Kashino et al. 2009, 2013). Given the complicated dynamics and unique features of large-scale variations of the ocean circulation near the western boundary in the tropical Pacific Ocean (Qiu and Joyce 1992; Qu and Lukas 2003; Kashino et al. 2011; Li et al. 2012; Liu and Zhou 2020; Liu et al. 2021), observing the structure and variability of the NECC in its source area will promote our understanding of the ocean dynamics and air–sea interactions in the tropical Pacific.

Since 2010, multiple open research cruises funded by the Ship Time Sharing Project of the National Natural Science Foundation of China (NSFC) have been conducted by the Institute of Oceanology, Chinese Academy of Sciences to survey the northwestern Pacific Ocean every year. Among them, three cruises were carried out across the NECC along the 130°E transect during the summer/fall of 2014, 2015, and 2016 (Table 1). During these three years, the widely anticipated major 2014/15 El Niño event failed to materialize but helped push the 2015/16 El Niño event to extreme magnitude (Levine and McPhaden 2016). This particularly strong El Niño has been generally considered to be comparable to another extreme event—the 1997/98 El Niño. Since extreme El Niños stand out not only for their powerful impacts but also for their

TABLE 1. Summary of cruises in the source area of the NECC in the far western Pacific Ocean, and MN represents the transect between Mindanao Island and New Guinea Island.

Cruise	Ship	Time	130°E	MN	8°N	Niño-3.4
KX14	R/V *Kexue*	25 Aug–8 Sep 2014	CTD	XCTD	XCTD	0.26
KX15	R/V *Kexue*	17–25 Sep 2015	CTD, SADCP, LADCP	XCTD, SADCP	XCTD, SADCP	2.01
KX16	R/V *Kexue*	28 Sep–8 Oct 2016	CTD, SADCP, LADCP	XCTD, SADCP	XCTD, SADCP	−0.61

significantly different properties and underlying dynamics from other El Niños (Levine and McPhaden 2016; Paek et al. 2017), observations of ocean condition during extreme events are very valuable for our understanding about their diversity and nature.

The implementation of Argo project in the world's oceans can sample the oceans synchronously and continuously at basin scales. These data provide comprehensive and continuous observations of the NECC in the far western Pacific Ocean. This paper employs in situ repeated hydrographic data, Argo, altimeter data, and reanalysis data to describe the structures and variations of the NECC at its birthplace during the 2014–16 El Niño. Meanwhile, comparisons of the NECC structure and variability in the far western Pacific Ocean (130°–160°E, 3°–7°N) between the 1997/98 and the 2015/16 super El Niño events and the underlying dynamics are also discussed.

Data and methodology used in this study are described in section 2. Section 3 provides the NECC structure and variability associated with the 2014–16 El Niño from observations, and section 4 investigates the structure and variability of the NECC during the 1997/98 and the 2015/16 El Niños associated with the causes and underlying dynamics. Summaries and conclusions are presented in the final section.

2. Data and methods

The repeated hydrographic data along the 130°E transect in this study were collected during three research cruises carried out on R/V *Kexue* during 2014–16 near the western equatorial Pacific Ocean (Figs. 1b–d). The information about these cruises is listed in Table 1. The periods of these cruises in the NECC region are 25 August–8 September in 2014 (cruise KX14), 17–25 September in 2015 (cruise KX15), and 28 September–8 October in 2016 (cruise KX16), respectively. These research cruises used a conductivity–temperature–depth profiler (CTD; SeaBird 911 plus by Sea Bird electronics) to measure ocean temperature and salinity profiles. Full-depth CTD casts at 1° intervals were made along 130°E between 2° and 13°N from the surface to the depth of about 50 m above the seafloor. The XCTD observations were conducted along the 8°N and the Mindanao to New Guinea (MN) sections from the surface to a depth of about 1000 m (Figs. 1b–d).

During the KX15 and KX16 cruises, upper-1000-m ocean current measurements were made throughout the whole voyage, using the shipboard ADCP (SADCP) at a frequency of 38 kHz that was installed on the R/V *Kexue*. The bin size of SADCP was 32 m with the first bin at 49.52 m. Meanwhile,

lowered acoustic Doppler current profiler (LADCP) measurements were made on CTD stations during these two cruises with a pair of Sontek 250-kHz ADCPs, which share the same depth range as the CTD measurements. The upward-looking and downward-looking instruments were configured to ping simultaneously about 3 times per second. The ping length was 16 m, and velocities were estimated in 8-m cells. Velocity profiles were calculated following the method described by Fischer and Visbeck (1993), which includes integrating shear from the bottom, combing bottom track information, and SADCP information. The LADCP measurements can provide a more accurate estimation of the NECC's transport compared with the SADCP due to its direct measurements of the upper-50-m velocity.

The daily gridded products of merged absolute dynamic topography heights (MADT-H) and absolute geostrophic velocities (MADT-UV) are used to provide context for the large-scale conditions in the western Pacific during the 2015/16 and the 1997/98 events. This dataset is provided by Aviso+ (http://www.aviso.altimetry.fr) and Copernicus Marine Environment Monitoring Service (CMEMS; http://marine.copernicus.eu/). The time period is from January 1993 to December 2016 with a spatial resolution of 0.25° × 0.25°. We also use the hydrographic data provided by Japan Agency for Marine-Earth Science and Technology (JAMSTEC; http://www.data.jma.go.jp/gmd/kaiyou/db/mar_env/results/OI/137E_OI_e.html) along the 137°E transect to do the comparison with the 1997/98 event. The monthly averaged temperature and salinity data during 2004–17 from the dataset of Global Gridded NetCDF Argo only dataset produced by optimal interpolation (Roemmich and Gilson 2009; http://doi.org/10.17882/42182) are used to derive the seasonal and interannual anomalies of the geostrophic velocity of the NECC at the 130°E transect. A 500–2500-day bandpass filter is applied to the monthly geostrophic velocity anomalies to present the interannual variations during 2014–16 in the NECC.

The monthly reanalyzed products of ocean velocity provided by European Centre for Medium-Range Weather Forecasts (ECMWF) Ocean Reanalysis system 4 (ORAS4; http://apdrc.soest.hawaii.edu/datadoc/ecmwf_oras4.php) (Balmaseda et al. 2013) from 1958 to 2017 are used to investigate the interannual variability of the NECC associated with different phases of the 1997/98 and 2015/16 El Niño events in the far western Pacific Ocean. The spatial resolution of ORAS4 is 1° × 1° in horizontal with 42 levels in vertical. The monthly climatology geostrophic transport of the NECC at the 130°E transect is calculated from the *World Ocean Atlas 2013* (*WOA13*; Boyer et al. 2013; https://www.nodc.noaa.gov/OC5/woa13/).
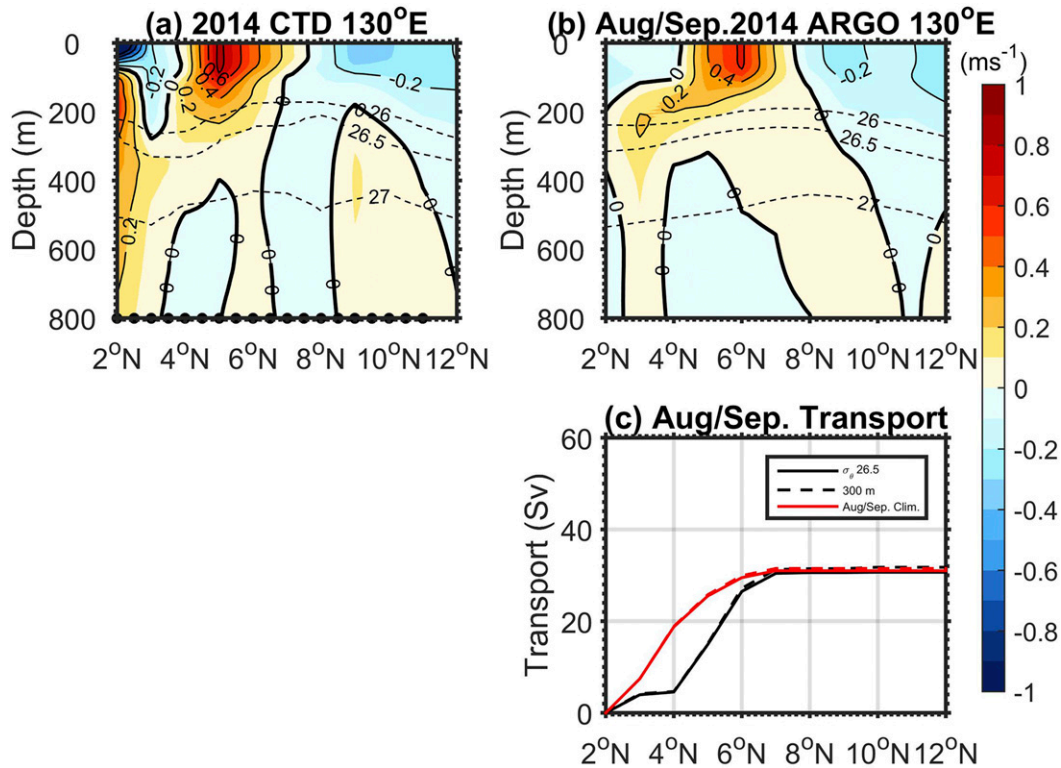
FIG. 2. Latitude–depth sections of zonal geostrophic velocities (m s^{-1}) calculated from (a) CTD observations, and (b) Argo data along the 130°E transect during the 2014 cruise with a reference level of 1500 m. The black dots along the bottom x axis in (a) represent the CTD stations. (c) The eastward transport (Sv) integrated from 2° to 12°N above 300 m (dashed line) and 26.5σ_θ (solid line) along the 130°E. The black and red lines represent the transports during the 2014 cruise and the monthly climatology of August–September from *WOA13* data, respectively.

The central latitude (Y_{CM}) and intensity (INT) of the whole-depth NECC (from the surface to 26.5σ_θ) are calculated from the monthly data of ORAS4 as follows (Hsin and Qiu 2012; TZ18):

$$Y_{CM}(x,t) = \frac{\int_{z=DR_{26.5}}^{z=0} \int_{Y_S}^{Y_N} yu(x,y,z,t)\, dy\, dz}{\int_{z=DR_{26.5}}^{z=0} \int_{Y_S}^{Y_N} u(x,y,z,t)\, dy\, dz}, \quad \text{and} \quad (1)$$

$$INT(x,t) = \int_{z=DR_{26.5}}^{z=0} \int_{\max(Y_{CM}-4^\circ,2^\circ N)}^{Y_{CM}+4^\circ} u(x,y,z,t)\, dy\, dz, \quad (2)$$

where x, y, and z are the longitude, latitude, and depth, respectively; Ys and Y_N are defined as 2° and 10°N as the northern and southern limits of the integration. The quantity u is the eastward current velocity, $DR_{26.5}$ is the depth corresponding to the lower boundary at the 26.5σ_θ density level. A 500–2500-day bandpass filtering is applied to highlight their fluctuations on the ENSO time scales.

The horizontal shears are calculated by averaging the absolute values of the meridional gradient of the zonal velocities between 3° and 7°N, and the vertical shears are calculated by differencing the mean zonal velocities between 0 and 300 m and those between 300 and 700 m using the same resolution as the observed or reanalysis data. The necessary condition for

baroclinic instability evaluated by a 2.5-layer reduced-gravity model is (see the appendix):

$$U_1 - (1+\gamma)U_2 > \gamma\lambda^2\beta, \quad (3)$$

where U_1, U_2 is the mean zonal flow in the surface and second layer, respectively. $\gamma = (\rho_2 - \rho_1)/(\rho_3 - \rho_2)$ is the stratification ratio, and $\lambda = (1/f_0)\sqrt{[(\rho_3 - \rho_2)/\rho_0]gH_2}$ is the internal Rossby radius, f_0 the Coriolis parameter at the reference latitude 5°N, and ρ_0 the reference density, g the acceleration of gravity, H_2 the second layer thickness, and the density in each layer is ρ_n ($n = 1, 2,$ and 3). Also, β is the meridional gradient of the planetary vorticity. Equation (3) can also be served as a sufficient condition for the current system with $U_1 - U_2 > 0$ (Qiu and Chen 2004).

3. Spatial and temporal variations of the NECC during 2014–16

a. Current across the 130°E section from hydrographic observations

We first use the repeated in situ observations across the NECC during KX14, KX15, and KX16 cruises to investigate the current structure in its source area in the far western Pacific Ocean (Figs. 2–4). The zonal velocities derived from the geostrophic equation (with the reference level of 1500 m), the
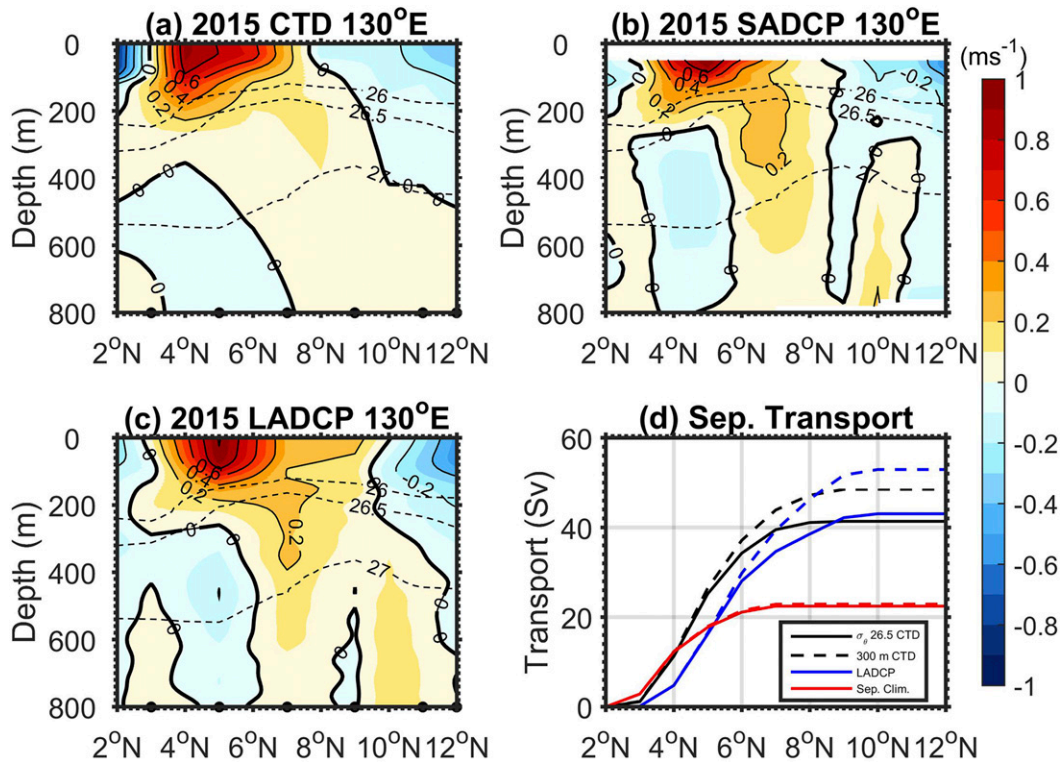
FIG. 3. Latitude–depth sections of (a) zonal geostrophic velocities (m s^{-1}) calculated from CTD observations with the reference level of 1500 m, (b) SADCP-measured zonal current, and (c) LACDP-measured zonal current along 130°E during the 2015 cruise. The black dots along the bottom x axis in (a) and (c) represent the CTD/LADCP stations. (d) The eastward transport (Sv) integrated from 2° to 12°N above 300 m (dashed line) and $26.5\sigma_\theta$ (solid line) along the 130°E transect, and the black and blue lines represent the transports derived from CTD and LADCP measurements during the 2015 cruise, respectively, and red lines the monthly climatology of September from *WOA13* data.

SADCP measurements, and the LADCP measurements along the 130°E section are combined to describe the spatial and temporal variability of the currents. Unfortunately, the SADCP and LADCP measurements during the KX14 cruise are not available, so we calculate the mean geostrophic flow during August–September 2014 from Argo data, and compare it with the CTD observations (Figs. 2b,c). The monthly climatology transport of the NECC along the 130°E transect derived from *WOA13* data is used to do the comparison with those from CTD or Argo observations.

The NECC was the dominant flow in the surface among all cruises, and it flowed eastward between 3° and 8°N above $26.5\sigma_\theta$, which corresponds to about 300 m here. It was strongest and deepest in 2015 with the maximum velocity exceeding 0.90 m s^{-1} at 5°N and the isoline of 0.20 m s^{-1} extending to 200 m (Figs. 3a–c). It was weakest and shallowest during the 2016 cruise with the 0.20 m s^{-1} isoline being shallower than 100 m (Figs. 4a–c). The current structure derived from Argo data in the synchronous months during the three cruises also demonstrated a consistent variation of the NECC with that of the in situ observations (Fig. S1 in the online supplemental material). Both show interannual variation related to ENSO as seen in other studies, that is, strong in El Niño years and weak

in La Niña years. This can also be verified from the geostrophic transports of the main body of the NECC above $26.5\sigma_\theta$ between 3° and 7°N during these three cruises (Figs. 2c, 3d, and 4d).

During the KX14 cruise, the transport of the NECC was about 29 Sv, which is close to its monthly climatology value of 30 Sv (Fig. 2c), consistent with the undeveloped El Niño state in 2014. In 2015, the transport above $26.5\sigma_\theta$ increased to 41 Sv, which is almost double its monthly climatology value (Fig. 3d). Moreover, the transport increased to 48 Sv if we integrate above 300 m. The total transports derived from LADCP measurements were a little larger than those from the CTD measurements. The difference between the $26.5\sigma_\theta$ and 300-m integrated transports is caused by the shoaling of the $26.5\sigma_\theta$ density level to less than 200 m north of 4°N during the 2015 cruise (Fig. 3a). This shoaling is consistent with the strong upwelling of the enhanced Mindanao Dome during El Niño events as suggested by previous studies (Tozuka et al. 2002; Kashino et al. 2011). In 2016, the NECC's transport decreased to its monthly climatology value of 20 Sv (Fig. 4d), corresponding to the decay phase of the 2015/16 El Niño. North of the NECC, all observations showed westward flow with the speed of 0.10–0.40 m s^{-1}, which seems to be the combination of
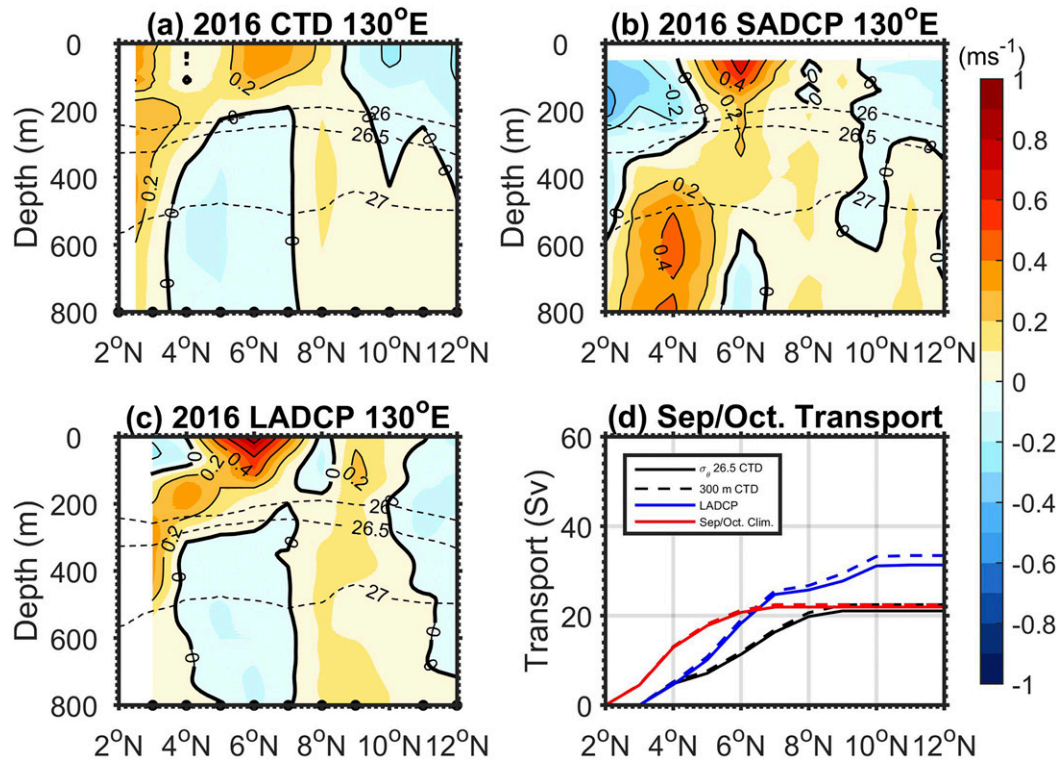
FIG. 4. As in Fig. 3, but for the 2016 cruise. Red lines in (d) are monthly climatology of September–October, and the eastward transport is integrated from 3°N for the CTD and LADCP measurements.

the northern part of the ME and the NEC. It was much stronger in 2014 and 2015 than that in 2016, which is consistent with the enhancement of the tropical gyre during the developing phase of El Niño (Qiu and Chen 2012), although the 2014 El Niño is an undeveloped one.

The subsurface currents showed more vigorous variability than the surface currents during these three cruises. All of them showed the westward North Equatorial Subsurface Current (NESC) between 3° and 5°N under the NECC with different widths and vertical extent. The NESC was much stronger during the KX15 cruise with its maximum speed exceeding 0.13 m s^{-1} around 400–600-m depth in both SADCP and LADCP measurements (Figs. 3a,b), suggesting its intensification during the 2015/16 El Niño event as revealed by subsurface moorings deployed between 0°and 7.5°N at 142°E during August 2014–October 2015 (Song et al. 2018). The subsurface currents also showed that the lower NECC shifted equatorward with depth, and it connected with the eastward-flowing North Subsurface Countercurrent (NSCC) below 100 m south of 4°N (Qiu and Joyce 1992; Gouriou and Toole 1993). The NSCC appeared to be the weakest during the KX15 cruise (Fig. 3a) and the strongest during the KX16 cruise (Fig. 4a). There were also two eastward flows centering at 6°–7°N and 9°–10°N below 300 m from the SADCP and LADCP measurements during the KX15 cruise, which may correspond to the southern branch of the North Equatorial Undercurrent (NEUC). Their speeds exceeded 0.10 m s^{-1}, which is much stronger than the value of 0.04–0.05 m s^{-1} calculated from

12-yr mean Argo data by Qiu et al. (2013), especially at 6°–7°N, where the velocities reach 0.20 m s^{-1} with its core shoaling to 300 m and connecting with the NECC (Figs. 3a,b). The enhancement of the southern branch of NEUC in 2015 may result from the eastward flow of the south part of the much stronger ME during the El Niño state (Figs. 3a–c and 5a–d; Kashino et al. 2011).

It is worth noting that there are also some differences among the current structures calculated from the geostrophic equation, the SADCP, and LADCP measurements during both the KX15 and KX16 cruises. These differences may indicate the high variability of the ocean circulation due to the meridional shift of the HE and the ME in this region. One notable example is that the total transport derived from the LADCP measurements is about 10 Sv larger than the geostrophic transport from the CTD measurements, which may relate to a transient enhancement of HE during the KX16 cruise (Fig. 5d). We further demonstrate the averaged velocities between 50 and 300 m from the SADCP observations in Figs. 5a and 5b. The KX15 cruise showed a strong eastward flow along 130°E transect between 3° and 8°N with the maximum velocity being located around 5°N (Fig. 5a). This flow may be traced back to a northeastward flow along the north part of the MN section, which corresponds to the anticyclonic meandering of the NECC as revealed in altimeter data (Fig. 5c).

Different from the KX15 cruise, the current vectors along the 130°E transect during the KX16 cruise were northeastward between 6° and 8°N, it shifted southeastward to the south of
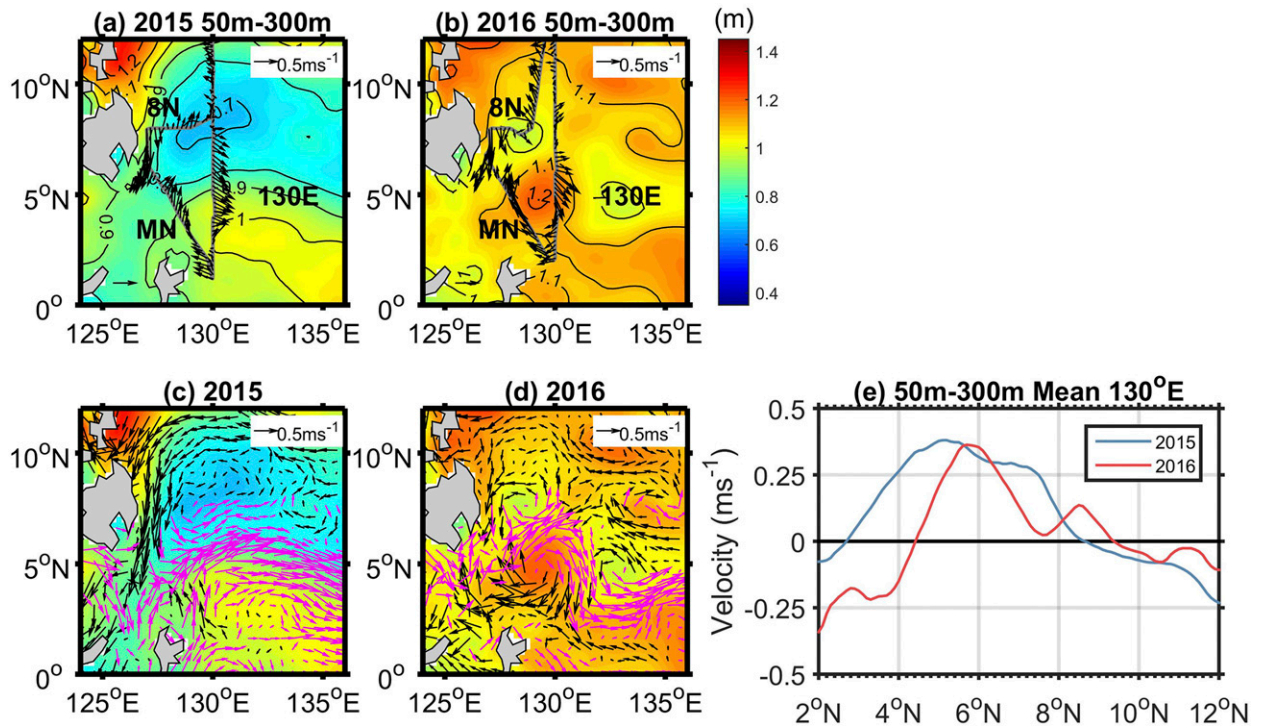
FIG. 5. SADCP currents (m s^{-1}; arrows) averaged between 50 and 300 m during the (a) 2015 cruise and (b) 2016 cruise. The color shadings represent the mean absolute dynamic height (m) during the two cruises. (c),(d) As in (a) and (b), but for the mean absolute geostrophic current at the surface, and the purple arrows represent vectors containing eastward velocity and black arrows westward velocity. (e) The latitudinal distribution of zonal velocity averaged between 50 and 300 m along the 130°E transect during the 2015 (blue line) and 2016 (red line) cruise.

6°N (Fig. 5b), which suggests an anticyclonic rotation of the current direction from the north to the south. The westward flows south of 4°N along 130°E and the northwest–northeastward flow along the MN section clearly showed the strong anticyclonic HE (Figs. 5b,d), and its center was located around 5°N, 129.5°E. Meanwhile, the ME during KX15 was much stronger and offshore compared with that during KX16. During KX15, it was centered around 7.5°N, 130°E with a band of low absolute dynamic height (ADT; <0.7 m) extending from 128° to 131°E in the northeast–southwestward direction (Fig. 5a). It shrank westward centering around 7.5°N, 128.3°E with a diameter of 170 km occupied by a much elevated ADT (1.0 m) during the KX16 (Fig. 5b). The distinct flow pattern during the two cruises suggests that an intensified northwestward shifting HE and a weakened nearshore shifting ME may occur during the decay phase of El Niño, whereas the developing phase of El Niño may relate to a much weaker HE and a stronger ME. The NECC in this region is largely shaped by the two eddies and may play a quite different role in the warm water advection during different phases of the ENSO. The observed features of the ME and the HE during KX15 and KX16 were consistent with their interannual variability as revealed by Kashino et al. (2013).

We further plot the latitudinal distribution of zonal velocity averaged between 50 and 300 m along the 130°E transect from SADCP measurements (Fig. 5e). Although the maximum

velocities of the NECC were comparable during the two cruises, the NECC was located between 4.5° and 7.5°N with the maximum speed centering around 6°N during the KX16 cruise, and it was located between 2.7° and 8.5°N with the maximum speed centering around 5°N during the KX15 cruise. The 1° southward shift and increase of the meridional width of the NECC during the KX15 cruise also demonstrated the significant influence of the 2015/16 El Niño on the ocean circulation in the far western Pacific Ocean.

b. Results from Argo observations

The interannual geostrophic velocity anomaly (GVA) time series during 2014–16 is calculated from Argo data at 5°N along the 130°E transect (Fig. 6a). The time range of the GVA is chosen to cover the time windows of the three cruises, and the latitude is chosen to represent the main axis of the NECC at its birthplace. Here the GVA is defined as the deviations from the monthly climatology geostrophic velocity, which is calculated from the Argo data during 2004–17. The GVA time series is detrended, then, 500–2500-day bandpass filtered to get the interannual variation.

At 5°N, where the main axis of the NECC is located, the eastward anomalies were dominant from March 2014 to March 2016, which corresponds to the enhancement of the current during the 2014–16 El Niño (Fig. 6a). The eastward anomalies were much stronger from June to December in 2015,
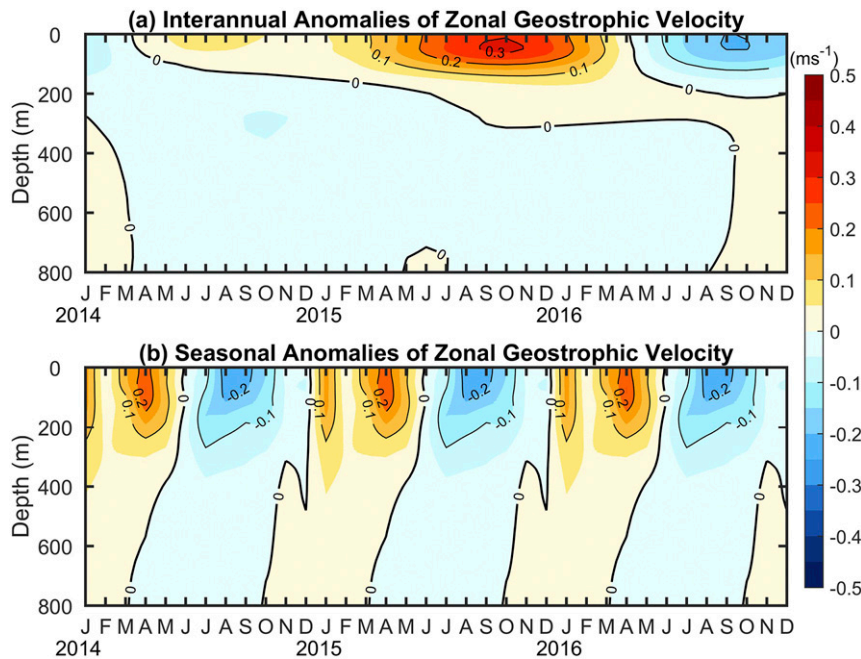
FIG. 6. (a) 500–2500-day bandpassed anomalies and (b) seasonal anomalies of zonal geostrophic velocity (m s^{-1}) from Argo observations at 5°N along 130°E. The reference level for geostrophic velocity is 1500 m, and the seasonal cycle is replicated three times to compare with the interannual anomalies in (a).

when the 2015/16 El Niño was developing and peaked. After the peak phase, the eastward anomalies decreased significantly and turned into westward anomalies from April to December in 2016. These eastward/westward anomalies indicated the strengthening/weakening of the NECC during the developing/decaying phase of the 2015/16 El Niño event, which is consistent with our synoptic hydrographic observations described in previous sections.

Since the NECC also has very strong seasonal variations, to compare the amplitudes of the seasonal and interannual anomalies, we present the seasonal GVA of the NECC derived from 14-year-long Argo data around its main axis (Fig. 6b). The NECC along the 130°E section is characterized by being weak from June to November and strong from December to the next May, and the seasonal minima/maxima occur in August/March with the anomalies exceeding 0.2 m s^{-1}. It is worth noting that the maximum eastward GVA exceeded 0.3 m s^{-1} during the peak phase in 2015 late fall, which was out of phase with its seasonality with a larger amplitude compared with that of the seasonal anomaly. This indicates the significant effects of the 2015/16 El Niño on the variation of the NECC at the 130°E transect in the far western Pacific Ocean.

4. Comparison with the 1997/98 event

The recent 2015/16 El Niño was exceptionally strong and is considered comparable to the extreme 1997/98 El Niño. However, the dynamics of these two extreme events are considered to be different. The 1997/98 event was generated by the traditional ENSO dynamics with SST anomalies in the

equatorial eastern Pacific being controlled by the thermocline feedback (e.g., Wyrtki 1975; Suarez and Schopf 1988; Battisti and Hirst 1989; Jin 1997), which is classified as eastern Pacific (EP) El Niño. The dynamics of the 2015/16 event was a little more complex. In addition to the thermocline feedback, the forcing from the subtropical atmosphere also played an important role in its evolution, and it is classified as a mixture of EP and central Pacific (CP) El Niño events, with the CP index dominant (Paek et al. 2017). It has been suggested that the different dynamics of the two types of El Niño may produce distinct impacts on the NECC. Hsin and Qiu (2012) first concluded that the EP-El Niño exerts a significant impact on the NECC, whereas the CP El Niño has little influence. TZ18 pointed out that their conclusion was biased by using two highly dependent ENSO indexes to classify the El Niño types (Kao and Yu 2009; Ren and Jin 2011) and concluded that both types of El Niño can exert significant but different impacts on the interannual variations of the NECC, that is, the variations are confined in the central-eastern Pacific for the EP type and the western-central Pacific for the CP type.

a. Comparison along the 137°E transect from hydrographic observations

To investigate the distinct variations of the NECC in the far western Pacific Ocean during the two extreme events, we compare the structure of the NECC by using hydrographic data in 1997 along the 137°E section provided by JAMSTEC. These data were obtained in October 1997, which is one month before the peak phase of 1997/98 event, so we calculate the geostrophic flow along the same section in November 2015 by
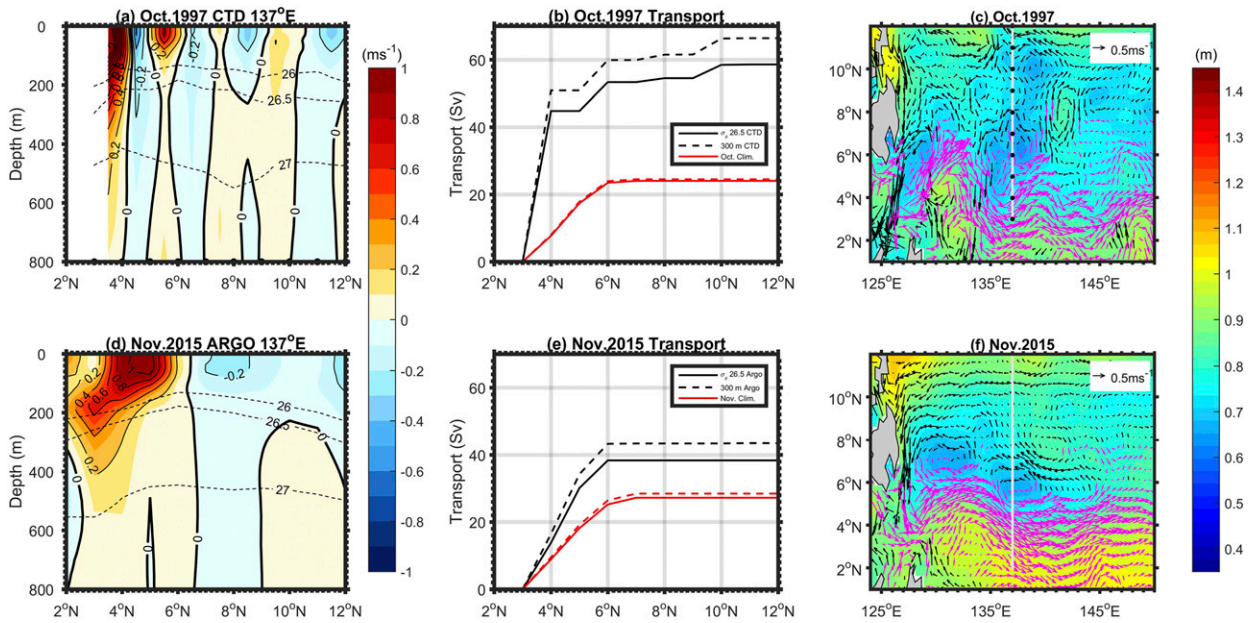
FIG. 7. (a) Latitude–depth section of zonal geostrophic velocities (m s^{-1}) in October 1997 along the 137°E section from CTD observations. (b) The eastward transport (Sv) integrated from 3° to 12°N above 300 m (black dashed line) and 26.5σ_θ (black solid line) along the 137°E section in October 1997, and the red lines represent the monthly climatology of October. (c) Absolute dynamic height (m) and absolute geostrophic currents (m s^{-1}) in October 1997 from altimeter data. (d)–(f) As in (a)–(c), but for geostrophic velocities calculated from Argo data in November 2015, and the red lines in (e) represent the monthly climatology of November. The purple arrows represent vectors containing eastward velocity and black arrows westward velocity in (c) and (f).

using Argo data, which is also one month before the peak phase of 2015/16 event, to do the comparison during the same phase of the two extreme events (Fig. 7).

The eastward geostrophic flow south of 7°N in October 1997 showed a very strong and deep core located south of 4°N and a shallow core centered at 5.5°N (Fig. 7a). The transport integrated above 300 m between 3° and 8°N was about 55 Sv (Fig. 7b), which doubles the monthly climatology value. The transport integrated above 26.5σ_θ, while weaker, still exceeded 50 Sv. The NECC in November 2015 showed a quite different structure from that in October 1997 with a broad and deep eastward flow south of 6.5°N and a maximum velocity exceeding 1.0 m s^{-1}. To the north of the NECC, there was a very strong westward flow between 6° and 9°N with the mean speed exceeding 0.20 m s^{-1} above 26.5σ_θ, the broad eastward/westward flow south/north of 6.5°N was in fact the southern/northern part of a cyclonic eddy, which was centered around (6.5°N, 137°E) as revealed by the altimeter data (Fig. 7f).

The lower part of the NECC connected with the NSCC south of 3°N below 200 m. The transport integrated above 300 m was about 44 Sv, smaller than that in October 1997 but much larger than the monthly climatology value of 28 Sv, suggesting the significant influence of the 2015/16 El Niño on the NECC. The large transport in October 1997 may result from the strong northeastward flow south of 4°N associated with temporal mesoscale meanders as indicated from simultaneous surface velocity fields derived from the altimeter data (Figs. 7c,d). The hydrographic observations along the 137°E transect suggest that the 2015/16 El Niño exerts significant

influence on the NECC with a comparable amplitude with that of the 1997/98 event in the far western Pacific Ocean.

b. Comparison from reanalysis data

Since the above hydrographic observations only provide a snapshot of the differences in the NECC containing signals from synoptic eddies or meanders during the two extreme El Niños, we further analyze these differences by using the ERA-S4 data from 1958 to 2017, which can investigate the interannual evolution of the NECC above 300 m (whole vertical range of the NECC). Figure 8 shows the anomalies of the interannual variation of NECC's central latitude (Y_{CM}) and intensity (INT) during the 1997/98 and 2015/16 El Niños, respectively. Month "0" indicates the peak month of each event. The southward (northward) shift and strengthening (weakening) of the NECC with comparable amplitude can be clearly identified during the developing (decaying) phase in both events, albeit the timing and location of the maximum variation of the INT and Y_{CM} differ from each other during the two events, which is generally consistent with the hydrographic observations.

During the developing phase (from −6 to 0 month), the INT anomalies (INTA) of the NECC in the 2015/16 El Niño showed a significant (compared to the mean during 1958–2017) strengthening with the 6-Sv isoline extending from 160° to 130°E, and the maximum value exceeding 10 Sv. However, it was much weaker in the 1997/98 El Niño, and the 6-Sv isoline was only confined to the east of 150°E. Meanwhile, the southward shift of Y_{CM} west of 140°E exceeded 0.6° in the 1997/98 event, which was much stronger than that in the 2015/16 event,
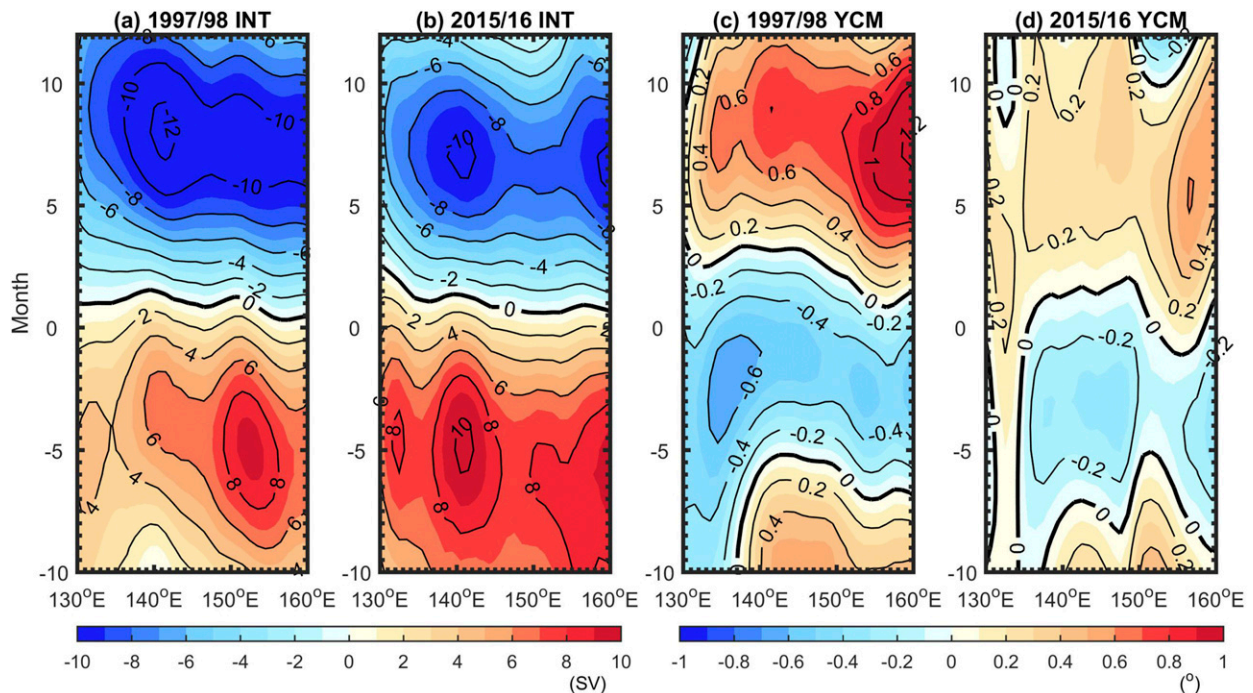
FIG. 8. Time–longitude plots of 500–2500-day bandpass anomalies of NECC's intensity (Sv) averaged between 3° and 7°N in the upper 300 m in the far western Pacific Ocean during (a) 1997/98 and (b) 2015/16 El Niño from ORAS4 product. (c),(d) As in (a) and (b), but for the latitude anomalies of the NECC's axis (°). Month ''0'' indicates the peak month of each event, and negative months indicate the developing phase.

suggesting the consistent feature of a much more twisted path of the NECC in the 1997/98 event as revealed from the altimeter data in Figs. 7a and 7c. However, the variation of the NECC Y_{CM} during these two extreme events did not show clear westward propagation signals, especially in the region west of 140°E for the 1997/98 event (Fig. 8c).

There were also distinct structures of the INT and Y_{CM} during the decay phase of the two extreme El Niños, both the INT and Y_{CM} in the 1997/98 decay phase showed much stronger amplitude compared with those in the 2015/16 event. This significant difference may attribute to the much stronger La Niña followed by the 1997/98 El Niño than that followed by the 2015/16 El Niño.

c. EKE and baroclinic instability

Previous studies have suggested that the interannual variation of the interior NECC is modulated by ENSO-related Rossby/Kelvin waves and Ekman pumping (Hsin and Qiu 2012; Zhao et al. 2013; TZ18). At the birthplace of the NECC, where more complicated dynamical processes such as pronounced local wind forcing, convergence of distinct water masses, ocean waves accumulation and reflection, and existence of the quasi-permanent eddies (HE and ME), the NECC's interannual variations are assumed to be more complex than its interior part. Eddies can impact the mean flow strength, structure, and stability (Düing et al.1975; Dewar and Bane 1989; Flament et al. 1996), and potentially act as a source of the interannual variability in the mean flow (Spall 1996; Qiu

2000; Roemmich and Gilson 2001). So understanding the interannual variabilities of the eddy kinetic energy (EKE) and its energy source is the key to understand the interannual variation of the NECC at its birthplace.

Zhao et al. (2013) found some consistency between the interannual variabilities of the EKE and INT of the NECC in the far western Pacific Ocean, and suggested that the horizontal shear may play an important role in transferring the kinetic energy from the mean flow to mesoscale eddies via barotropic instability. Qiu and Chen (2004) suggested that flows in the low-latitude ocean are unlikely to be subject to baroclinic instability, since a very large vertical shear is required to reverse the sign of the mean potential vorticity gradient in the subsurface layer due to the large local deformation radius [see Eq. (3)]. However, Zhao et al. (2013) also mentioned the inconsistency between the variations of INT and EKE in some events, suggesting that the barotropic instability cannot account for all interannual variations in the INT of the NECC.

The NECC–NESC system is consistent with the structure of zonal currents above the main thermocline with a surface-eastward/subsurface-westward flow, which is potentially unstable baroclinically (Qiu 1999). Moreover, from the above hydrographic data analyses during the 2015/16 and 1997/98 events, we can see very strong surface and subsurface currents with an opposite sign during these two events (recall Figs. 2–4). Given the complex dynamical processes in the far western Pacific NECC and its characteristics of highly time-dependent
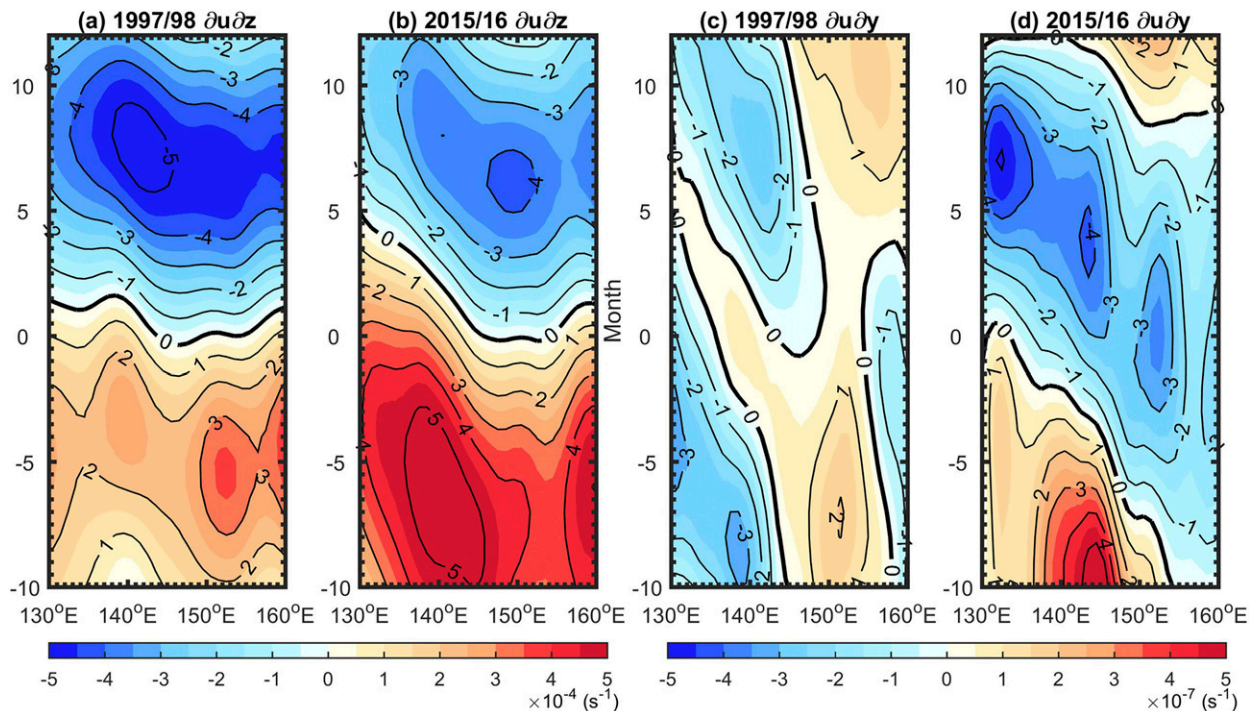
FIG. 9. Time–longitude plots of 500–2500-day bandpass anomalies of vertical shear (s^{-1}) averaged between 3° and 7°N of the NECC during (a) 1997/98 and (b) 2015/16 El Niño from ORAS4 product. (c),(d) As in (a) and (b), but for horizontal shear in the upper 300 m.

current with comparable speed fluctuations to its mean (Kashino et al. 2009; Zhao et al. 2013), baroclinic instability induced by strong vertical shear may also play an important role in modulating the EKE and INT of the NECC in this region.

Hence, we compare the horizontal versus vertical shears in the far western Pacific NECC during the 1997/98 and 2015/16 El Niños by using the monthly ORAS4 current data (Fig. 9). Although the 1° coarse resolution data will underestimate both types of shear, their interannual variations are not sensitive to the data resolution (Fig. S2). The vertical shears in both events show quite consistent variability with increase/decrease during the developing/decaying phases (Figs. 9a,b), albeit some phase lags in the 2015/16 event, which is consistent with the inter-annual variation of the NECC INT associated with ENSO. However, the amplitude of the vertical shear anomalies during the developing phase of 2015/16 El Niño was almost double that of 1997/98 especially west of 150°E with obvious westward propagation signals, suggesting the more significant influence on the western Pacific Ocean by the CP dominant mixed type 2015/16 El Niño as concluded by TZ18.

By contrast, the horizontal shears displayed a little complex variability in both events. In the developing phase of the 1997/98 El Niño, positive (negative) anomalies were dominant in the NECC east (west) of 142°E with obvious westward propagation signals, and the situation was reversed during its decay phase. As to the 2015/16 El Niño, the reversed horizontal shear showed large positive anomalies around 145°E about 10 months before its peak, and these positive anomalies propagated westward with their zonal width westward shrinking as the El Niño

developing. Meanwhile, negative anomalies east of 154°E propagated westward with their zonal width expanding. It is worth noting that variations of the two types of shear during the decaying phases of the 1997/98 and 2015/16 events seemed to be in the opposite situation, with much stronger vertical shears for the 1997/98 event and horizontal shears for the 2015/16 event (Fig. 9). A strong La Niña followed the 1997/98 El Niño, and a weak one followed the 2015/16 El Niño. Thus the two events differed fundamentally and the distinct variation of the hori-zontal and vertical shears during the developing and decaying phases of the two events may reflect their different dynamics. Analyses of these features are beyond the present study as we mainly focus on the developing phase.

To verify if the strong vertical shear can induce baroclinic instability of the NECC in the far western Pacific Ocean, we consider the vertically sheared NECC–NESC system in a 2.5-layer reduced-gravity model by using parameter values appropriate for the system listed in Table 2. The reference latitude for f_0 and β is taken at 5°N and the other parameter values are estimated from the monthly climatological datasets of ORAS4. We can see that ΔU, calculated from geostrophic velocity difference between the upper 300 and 300–700 m based on CTD observations, generally peaks between 3° and 7°N (Fig. 10a), where the NECC locates. It was much larger in 2014 and 2015 compared with that in 2016, which is consistent with the enhancement/decrease of the NECC during El Niño/La Niña state. The observed ΔU in all cruises exceeds the critical value U_c for baroclinic instability based on the necessary condition from Eq. (3) in the 2.5-layer model between 4.5° and 6.5°N, albeit at different latitudes, indicating that the NECC

TABLE 2. Parameter values appropriate for the NECC–NESC system for the 2.5-layer reduced gravity model.

Parameter	Value
f_0	$1.27 \times 10^{-5} \, \mathrm{s}^{-1}$
β	$2.28 \times 10^{-11} \, \mathrm{m}^{-1} \, \mathrm{s}^{-1}$
U_1	$0.8 \, \mathrm{m \, s}^{-1}$
U_2	$-0.15 \, \mathrm{m \, s}^{-1}$
H_1	$300 \, \mathrm{m}$
H_2	$400 \, \mathrm{m}$
ρ_1	$25.50\sigma_\theta$
ρ_2	$26.50\sigma_\theta$
ρ_3	$27.75\sigma_\theta$
γ	0.8
$2\pi/l$	$800 \, \mathrm{km}$
ΔU	$0.95 \, \mathrm{m \, s}^{-1}$
$\gamma\lambda^2\beta + \gamma U_2$	$0.80 \, \mathrm{m \, s}^{-1}$

is subject to baroclinic instability at these latitudes. It is worth noting that the U_c is also served as a sufficient condition for the baroclinic instability as the NECC–NESC system meets the condition of $U_1 - U_2 > 0$ (Qiu and Chen 2004). The ΔU based on SADCP and LADCP measurements in 2015 and 2016 also confirm the potential baroclinic instability of the NECC (Fig. 10c).

The above analyses suggest that the vertical shears in the NECC along the 130°E transect during the three cruises in 2014–16 can exceed the critical values of the necessary and sufficient condition based on the 2.5-layer reduced-gravity model for baroclinic instability. Although the local deformation radius is large in the NECC–NESC latitudinal bands, which requires a much larger vertical shear to reverse the sign of the mean potential vorticity gradient in the subsurface layer. The westward NESC causes the mean potential vorticity gradient in the subsurface layer to have an opposite sign (i.e., negative) from that in the surface eastward NECC layer, rendering the vertically sheared NECC–NESC system to be

baroclinically unstable. The quasi-permanent HE can also contribute to the vigorous vertical shears in this region (recall Figs. 5c,d; Kashino et al. 2013).

Meanwhile, during El Niño developing phase, the enhanced vertical velocity shear associated with the enhancement of the NECC and the reduced stratification between the NECC layer (upper 300 m) and the subsurface NESC layer (300–700 m) in the western Pacific Ocean help the system meet the necessary and sufficient condition for baroclinic instability (Fig. 11). In short, both geostrophic currents derived from the CTD measurements and direct currents measured by SADCP and LADCP along the 130°E transect across the NECC during 2014–16 suggest that the NECC here is baroclinically unstable during the observation period.

Since the EKE generally drains energy from the mean flow, previous studies mainly emphasize the influence of barotropic instability on the EKE of the NECC in this region (Zhao et al. 2013; Hsin and Qiu 2012), little attention has been paid to the contribution of baroclinic instability. Here we do the lag correlations between the interannual anomalies of EKE and the horizontal and vertical shears, respectively, to examine their relative contributions to the EKE field (Fig. 12).

As the horizontal scale of mesoscale eddies is generally related to, but somewhat larger than, the Rossby radius of deformation, here we use the ORAS4 product to calculate the EKE in the whole-depth NECC given the large deformation radius (~200 km) of the first baroclinic Rossby waves in the NECC latitudes. We first compare the interannual surface EKE anomalies between the ORAS4 product and the altimetry data during the two extreme El Niños to evaluate the errors caused by the 1° coarse resolution in ORAS4 product (Fig. 13). Here a Gaussian 400-km half-width filter is applied to the EKE anomalies derived from altimetry data in order to eliminate small scale features. Generally, the main pattern of the EKE with negative (positive) anomalies being dominant during the developing phase of 1997/98 (2015/16) El Niño can be identified from both ORAS4 product and altimetry data, albeit with
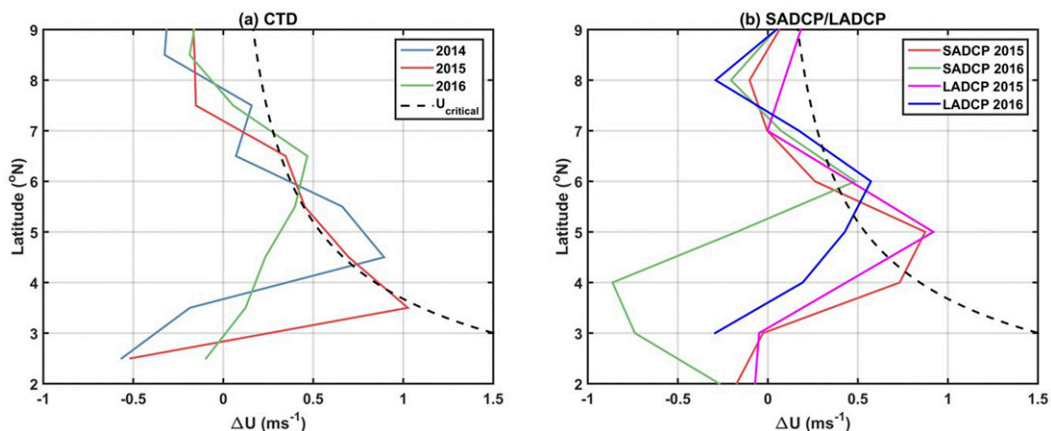

FIG. 10. The vertical velocity shears between the upper (0–300 m) and the lower (300–700 m) layers (colored solid lines) and critical value (black dashed line) of the necessary and sufficient condition for baroclinic instability predicted by 2.5-layer reduced-gravity model based on (a) the zonal velocity from synoptic hydrographic data collected during 2014–16 cruises along the 130°E transect and (b) LADCP and SADCP measurements.
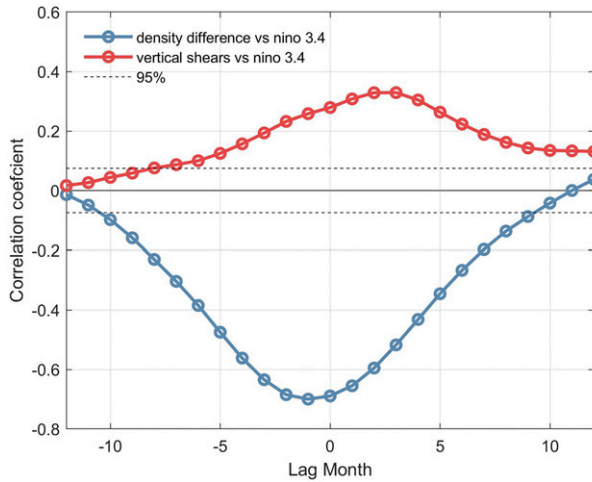
FIG. 11. Lag correlations between the Niño-3.4 index and the monthly anomalies of vertical shears (red) and the density jump between the NECC layer (upper 300 m) and the subsurface NESC layer (300–700 m; blue) along the 130°E transect based on ORAS4 product, respectively. Positive values indicate the Niño-3.4 index is lagged.

some discrepancies near the western boundary region. The comparison suggests that the ORAS4 product can capture the main characteristics of interannual anomalies of the EKE in this region. The EKE averaged in the upper 300 m basically

resembles its surface part but a smaller amplitude (Fig. S3). The distinct EKE evolution during the two extreme events also suggests the diverse eddy–mean flow interactions of the NECC in the far western Pacific Ocean in different El Niño events.

Since the shears in the far western Pacific Ocean demonstrate quite different spatial evolutions as revealed in Fig. 9, we divide the NECC into the western part [box 1: (3°–7°N, 130°–140°E)] and the eastern part [box 2: (3°–7°N, 141°–160°E)], and do the lag correlation for the two boxes, respectively (Figs. 12a,b). In both boxes, the vertical shears show a much higher lead correlation ($r > 0.47$) with the EKE than that of the horizontal shear ($r < 0.27$). In Fig. 14, we plot the phase speed c_r and the growth rate kc_i of the NECC–NESC system as a function of zonal wavenumber k based on the 2.5-layer model for the two boxes, respectively. Here we use the same parameters listed in Table 2 for the calculations except for the values of U_1, ρ_1, and γ, which are 0.65 m s^{-1}, 25.35ρ_θ, and 0.92 for box 2 given the decreased speed and shoaling of the NECC as it flows eastward (Johnson et al. 2002).

The most unstable mode has $kc_i = 0.028$ day^{-1}, corresponding to an e-folding time scale of 35.8 days. As shown in Fig. 12a, the maximum correlation between the vertical shear and the EKE occurs when the former leads the latter about 1 month in the western box, which is consistent with the e-folding time scale for the most unstable wave in this latitude as estimated by the 2.5-layer reduced gravity model (Figs. 14a,b). The leading month extends to about 90 days in the eastern box
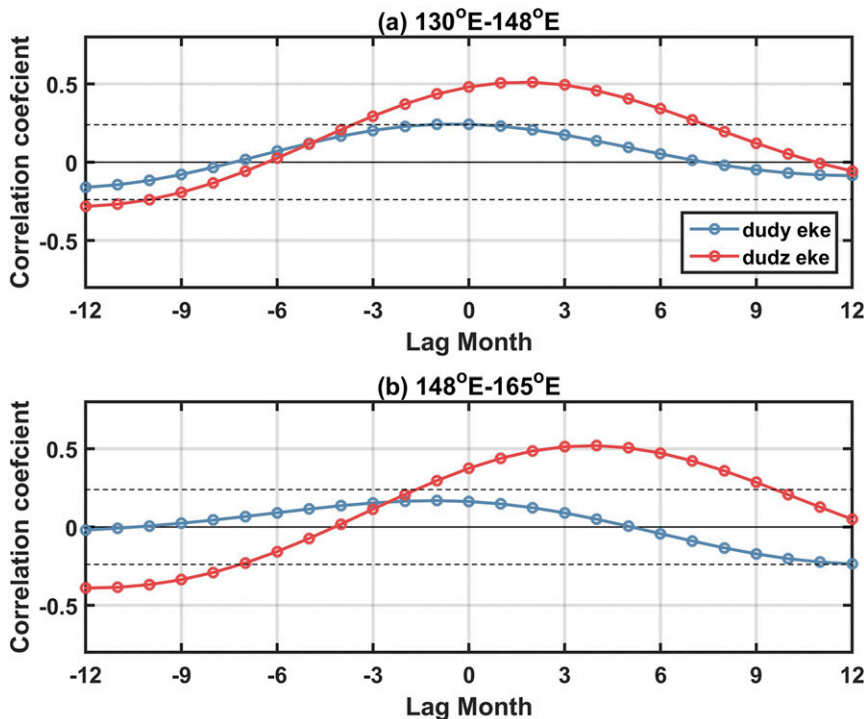

FIG. 12. The lag correlations between the 500–2500-day bandpassed anomalies of EKE and horizontal (blue)/vertical (red) shear averaged in (a) the western box (3°–7°N, 130°–140°E) and (b) the eastern box (3°–7°N, 141°–160°E) calculated from ORAS4 product. Positive months indicate the EKE is lagging. Black dashed lines mark the 95% confidence levels.
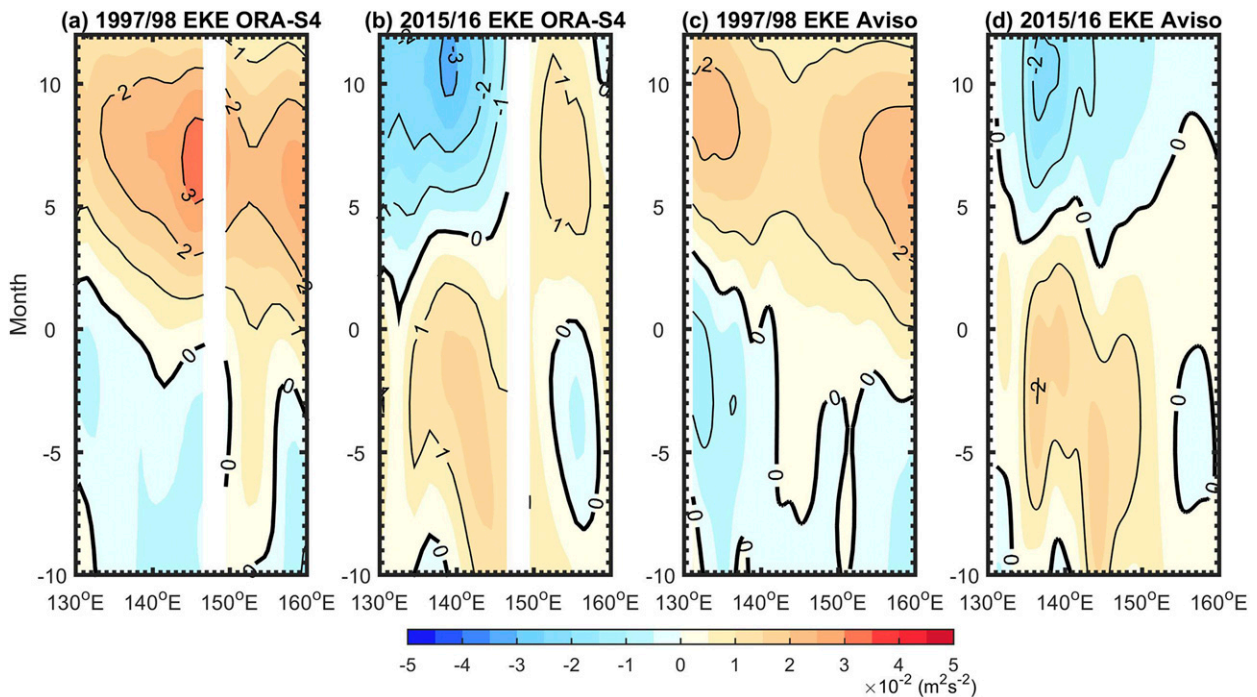
FIG. 13. Time–longitude plots of 500–2500-day bandpass anomalies of surface EKE during (a) 1997/98 and (b) 2015/16 El Niño calculated from ORAS4 geostrophic velocity averaged between 3° and 7°N. (c),(d) As in (a) and (b), but from altimeter data.

(Fig. 12b), which is also consistent with the *e*-folding time scale of 99.3 days calculated for the eastern box due to the decreasing speed of the NECC as it flowing to the east in the Pacific Ocean. The results of lag correlations between the interannual anomalies of EKE and horizontal/vertical shear indicate that the baroclinic instability could play a dominant role in the energy source of EKE in the source region of the NECC, which differs from the traditional understanding of the energy source of EKE as barotropic instability in low-latitude ocean. This result differs from that of Qiu et al. (2019), who argued that barotropic instability was the EKE energy source during the 2015/16 El Niño event at 3°–8°N and 130°–135°E based on Estimating the Circulation and Climate of the Ocean, Phase II (ECCO2), model output. Although both the ORAS4 and ECCO2 assimilate observational data, given the highly varied ocean currents and sparse observations in this region, the model output is dominated by the model behavior. As different models have different resolutions, data assimilation methods, parameterizations, and so on, the different conclusions about the energy source of EKE at the birthplace of the NECC by the above two datasets provides a strong motivation for adding to the regional in situ observations.

5. Summary and conclusions

The hydrographic data collected during three research cruises carried out on board of R/V *Kexue* during 2014–16, combined with the Argo data, altimetry data, and ORAS4 product in the western equatorial Pacific Ocean are used to investigate the structure and variability of the NECC at its

birthplace. The NECC here shifted ~1° southward and got intensified significantly, with its transport exceeding 40 Sv (1 Sv $\equiv 10^6 \, m^3 \, s^{-1}$), nearly a double of the climatology value, during the developing phase of the 2015/16 El Niño event. Its seasonality is characterized by being strong from December to the next May and weak from June to November. The strengthening of the NECC in the summer of 2015 was out of phase with its seasonality, suggesting the significant effects of the 2015/16 El Niño on the variation of the NECC in the far western Pacific Ocean.

Hydrographic data along the 137°E section provided by JAMSTEC and Argo data are used to examine variations of the NECC during the 1997/98 and 2015/16 extreme El Niño events. The transport integrated above 300 m during the 1997/98 El Niño was 3 times larger than climatology, with a value of about 58 Sv integrated between 3° and 8°N. This was about 10 Sv larger than that in the 2015/16 extreme El Niño. The simultaneous surface velocity field derived from altimeter data suggests that the path of NECC in the 1997/98 event was much more twisted with strong mesoscale meanders than that of 2015/16 event and may contribute to its large transport. Anomalies of interannual variations of the NECC's intensity obtained from ORAS4 product also suggest that the NECC was strong during the developing phase of the 2015/16 El Niño and comparable to that of the 1997/98 El Niño.

Analyses using the necessary and sufficient condition based on the 2.5-layer reduced-gravity model for baroclinic instability indicate that the NECC was baroclinically unstable during the 2014–16 cruise periods. The enhanced vertical velocity shear and the reduced density jump between the NECC and
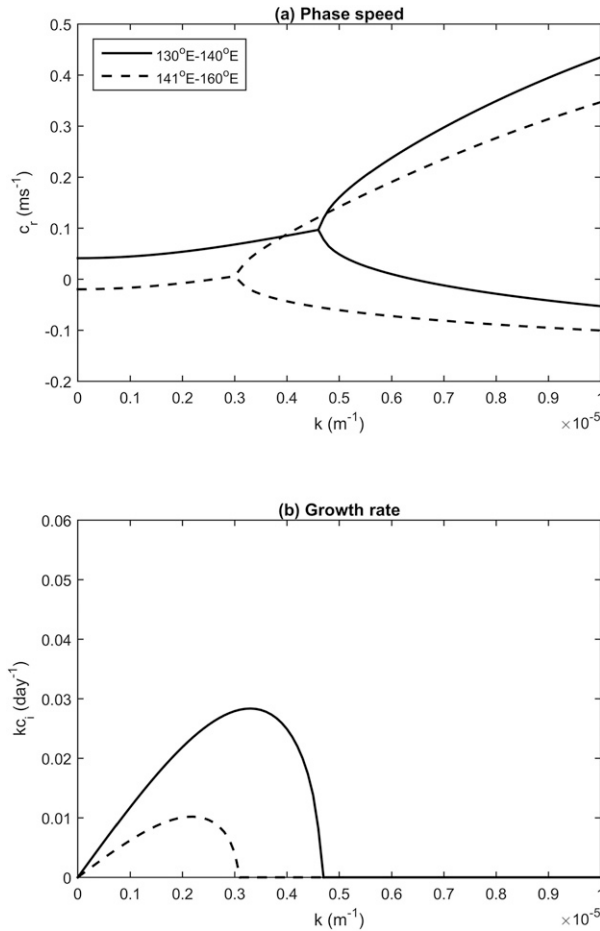
FIG. 14. (a) Phase speed and (b) growth rate as a function of zonal wavenumber k for the vertically sheared NECC–NESC system. Solid lines are for the west region (130°–140°E), and dashed lines are for the east region (141°–160°E).

the NESC during El Niño developing phase in the western Pacific Ocean helped the system meet the condition for the baroclinic instability.

In conclusion, our observations suggest that the CP dominant mixed type 2015/16 El Niño exerted a significant impact on the NECC in the far western Pacific Ocean, which was comparable to that of the 1997/98 EP type El Niño. The eddy–mean flow interactions in the NECC region in the western Pacific Ocean are highly variable associated with different El Niño events. During the 2015/16 El Niño, the NECC was a baroclinically unstable jet at its birthplace, and the baroclinic instability provided the main energy source for mesoscale eddy field. This result differs from the traditional understanding of the energy source of EKE in low-latitude ocean. The findings reported in this study contribute to advance our understanding of El Niño diversity and its impacts on the circulation and variability of the far western Pacific Ocean, especially for extreme El Niños.

APPENDIX

Conditions for Instability in a 2.5-Layer Model

In the surface layer, we assume the mean layer thickness is H_1 and the mean zonal flow is U_1, representing the eastward-flowing NECC. In the second layer, the mean layer thickness is H_2 and the mean zonal flow is U_2, which corresponds to the westward-flowing currents (i.e., NESC; Yuan et al. 2014; Wang et al. 2016). Below is a hypothetical quiescent, infinitely deep layer. The density in each layer is ρ_n ($n = 1$, 2, and 3).

Under the quasigeostrophic approximation, the linearized equations governing the perturbation potential vorticity q_n are

$$\left(\frac{\partial}{\partial t} + \frac{U_n \partial}{\partial x}\right) q_n + \frac{\partial \Pi_n}{\partial y} \frac{\partial \phi_n}{\partial x} = 0, \tag{A1}$$

where ϕ_n is the perturbation streamfunction and Π_n is the mean potential vorticity in the n layer ($n = 1$ and 2; see Pedlosky 1987).

Assuming the mean flow U_n is meridionally uniform, the perturbation streamfunction and the meridional gradient of Π_n in the 2.5-layer reduced-gravity model can be expressed by

$$q_1 = \nabla^2 \phi_1 + \frac{1}{\gamma \delta \lambda^2} (\phi_2 - \phi_1), \tag{A2}$$

$$q_2 = \nabla^2 \phi_2 + \frac{1}{\gamma \lambda^2} (\phi_1 - \phi_2 - \gamma \phi_2), \tag{A3}$$

$$\Pi_{1y} = \beta + \frac{1}{\gamma \delta \lambda^2} (U_1 - U_2), \quad \text{and} \tag{A4}$$

$$\Pi_{2y} = \beta - \frac{1}{\gamma \lambda^2} (U_1 - U_2 - \gamma U_2), \tag{A5}$$

where

$$\gamma = \frac{\rho_2 - \rho_1}{\rho_3 - \rho_2},$$

$$\delta = \frac{H_1}{H_2}, \quad \text{and}$$

$$\lambda = \frac{1}{f_0}\sqrt{\frac{\rho_3 - \rho_2}{\rho_0}gH_2}.$$

In the above equations, ∇^2 denotes the horizontal Laplacian operator, β denotes the meridional gradient of the Coriolis parameter, f_0 denotes the Coriolis parameter at the reference latitude, ρ_0 is the reference density, δ is the layer depth ratio, and γ is the stratification ratio.

By substituting the normal mode solution, $\phi_n = \mathrm{Re}[A_n e^{i(kx+ly-kct)}]$ into (A1) and using (A2)–(A5), we have

$$(U_1 - c)\left[-K^2 A_1 + \frac{1}{\gamma\delta\lambda^2}(A_2 - A_1)\right] + \Pi_{1y}A_1 = 0, \quad \text{and} \tag{A6}$$

$$(U_2 - c)\left[-K^2 A_2 + \frac{1}{\gamma\lambda^2}(A_1 - A^2 - \gamma A_2)\right] + \Pi_{2y}A_2 = 0, \tag{A7}$$

where $K^2 \equiv k^2 + l^2$ is the total wavenumber. Requiring non-trivial solutions for A_n leads to

$$c^2 - \left(U_1 + U_2 - \frac{P+Q}{R}\right)c$$
$$+ \left(U_1 U_2 + \frac{\Pi_{1y}\Pi_{2y}}{R} - \frac{U_1 P}{R} - \frac{U_2 Q}{R}\right) = 0, \tag{A8}$$

where

$$P = \left(K^2 + \frac{1}{\gamma\delta\lambda^2}\right)\Pi_{2y},$$

$$Q = \left(K^2 + \frac{1+\gamma}{\gamma\lambda^2}\right)\Pi_{1y}, \quad \text{and}$$

$$R = \left(K^2 + \frac{1+\gamma}{\gamma\lambda^2}\right)\left(K^2 + \frac{1}{\gamma\delta\lambda^2}\right) - \frac{1}{\gamma^2\delta\lambda^4}.$$

Multiplying (A6) and (A7) by $A_1 H_1/(U_1 - c)$ and $A_2 H_2/(U_2 - c)$, respectively, and adding them together, we get

$$K^2(H_1 A_1^2 + H_2 A_2^2) + \frac{H_2}{\gamma\lambda^2}(A_1 - A_2)^2 + \frac{H_2}{\lambda^2} + A_2^2$$
$$= \frac{H_1\Pi_{1y}}{U_1 - c}A_1^2 + \frac{H_2\Pi_{2y}}{U_2 - c}A_2^2. \tag{A9}$$

As both the real and imaginary part of (A8) must vanish separately, we have

$$c_i\left(\frac{H_1\Pi_{1y}}{|U_1 - c|}A_1^2 + \frac{H_2\Pi_{2y}}{U_2 - c}A_2^2\right) = 0 \tag{A10}$$

from the imaginary part. For the mode to be unstable ($c_i \neq 0$), (A10) indicates $\Pi_{1y}\Pi_{2y} < 0$, namely, the sign of the potential vorticity gradient of the mean state in the two active layers must be opposite. Since $U_1 - U_2 > 0$ in the NECC–NESC system, Π_{1y} is always positive [recall (A4)]. As such, the necessary and sufficient condition for instability is $\Pi_{2y} < 0$ (see Qiu and Chen 2004). By rewriting (A5) this leads to

$$U_1 - (1+\gamma)U_2 > \gamma\lambda^2\beta. \tag{A11}$$

Notice that the results of the above 2.5-layer reduced-gravity model reduce to those of the Phillips two-layer model if we take $\gamma \to 0$ and $\gamma\lambda^2 \to (\rho_2 - \rho_1)gH_2/\rho_0 f_0^2$ (Phillips 1951; Pedlosky 1987; Qiu 1999).

REFERENCES

Balmaseda, M. A., K. Mogensen, and A. T. Weaver, 2013: Evaluation of the ECMWF ocean reanalysis system ORAS4. *Quart. J. Roy. Meteor. Soc.*, **139**, 1132–1161, https://doi.org/10.1002/qj.2063.

Battisti, D. S., and A. C. Hirst, 1989: Interannual variability in a tropical atmosphere ocean model: Influence of the basic state, ocean geometry and nonlinearity. *J. Atmos. Sci.*, **46**, 1687–1712, https://doi.org/10.1175/1520-0469(1989)046<1687:IVIATA>2.0.CO;2.

Boyer, T. P., and Coauthors, 2013: *World Ocean Database 2013*. NOAA Atlas NESDIS 72, S. Levitus and A. Mishonov, Eds., 209 pp., http://doi.org/10.7289/V5NZ85MT.

Brown, J. N., J. S. Godfrey, and A. Schiller, 2007: A discussion of flow pathways in the central and eastern equatorial Pacific. *J. Phys. Oceanogr.*, **37**, 1321–1339, https://doi.org/10.1175/JPO3042.1.

Chen, X., B. Qiu, Y. Du, S. Chen, and Y. Qi, 2016: Interannual and interdecadal variability of the North Equatorial Countercurrent in the western Pacific. *J. Geophys. Res. Oceans*, **121**, 7743–7758, https://doi.org/10.1002/2016JC012190.

Clement, A. C., R. Seager, and R. Murtugudde, 2005: Why are there tropical warm pools? *J. Climate*, **18**, 5294–5311, https://doi.org/10.1175/JCLI3582.1.

Delcroix, T., G. Eldin, and C. Henin, 1987: Upper ocean water masses and transports in the western tropical Pacific (165°E). *J. Phys. Oceanogr.*, **17**, 2248–2262, https://doi.org/10.1175/1520-0485(1987)017<2248:UOWMAT>2.0.CO;2.

——, ——, M. H. Radenac, J. Toole, and E. Firing, 1992: Variation of the western equatorial Pacific Ocean, 1986–1988. *J. Geophys. Res.*, **97**, 5423–5445, https://doi.org/10.1029/92JC00127.

Dewar, W. K., and J. M. Bane, 1989: Gulf-stream dynamics. Part II: Eddy energetics at 73°W. *J. Phys. Oceanogr.*, **19**, 1574–1587, https://doi.org/10.1175/1520-0485(1989)019<1574:GSDPIE>2.0.CO;2.

Düing, W., and Coauthors, 1975: Meanders and long waves in equatorial Atlantic. *Nature*, **257**, 280–284, https://doi.org/10.1038/257280a0.

Fieux, M., C. Andrié, A. P. Delecluse, A. G. Ilahude, A. Kartavseff, F. Mantisi, R. Molcard, and J. C. Swallow, 1994: Measurements within the Pacific–Indian Oceans throughflow region. *Deep-Sea Res.*, **41**, 1091–1130, https://doi.org/10.1016/0967-0637(94)90020-5.

Fischer, J., and M. Visbeck, 1993: Deep velocity profiling with self-contained ADCPS. *J. Atmos. Oceanic Technol.*, **10**, 764–773, https://doi.org/10.1175/1520-0426(1993)010<0764:DVPWSC>2.0.CO;2.

Flament, P. J., S. C. Kennan, R. A. Knox, P. P. Niiler, and R. L. Bernstein, 1996: The three-dimensional structure of an upper ocean vortex in the tropical Pacific Ocean. *Nature*, **383**, 610–613, https://doi.org/10.1038/383610a0.

Gordon, A. L., 1986: Inter-ocean exchange of thermocline water. *J. Geophys. Res.*, **91**, 5037–5046, https://doi.org/10.1029/JC091iC04p05037.

——, and R. A. Fine, 1996: Pathways of water between the Pacific and Indian Oceans in the Indonesian Seas. *Nature*, **379**, 146–149, https://doi.org/10.1038/379146a0.

Gouriou, Y., and J. Toole, 1993: Mean circulation of the upper layers of the western equatorial Pacific Ocean. *J. Geophys. Res.*, **98**, 22 495–22 520, https://doi.org/10.1029/93JC02513.

Heron, S. F., E. J. Metzger, and W. J. Skirving, 2006: Seasonal variations of the ocean surface circulation in the vicinity of Palau. *J. Oceanogr.*, **62**, 413–426, https://doi.org/10.1007/s10872-006-0065-3.

Hsin, Y. C., and B. Qiu, 2012: The impact of eastern-Pacific versus central-Pacific El Niños on the North Equatorial Countercurrent in the Pacific Ocean. *J. Geophys. Res.*, **117**, C11017, https://doi.org/10.1029/2012JC008362.

Jin, F. F., 1997: An equatorial ocean recharge paradigm for ENSO. Part I: Conceptual model. *J. Atmos. Sci.*, **54**, 811–829, https://doi.org/10.1175/1520-0469(1997)054<0811:AEORPF>2.0.CO;2.

Johnson, G. C., B. M. Sloyan, W. S. Kessler, and K. E. McTaggart, 2002: Direct measurements of upper ocean currents and water properties across the tropical Pacific during the 1990s. *Prog. Oceanogr.*, **52**, 31–61, https://doi.org/10.1016/S0079-6611(02)00021-6.

Kao, H., and J. Yu, 2009: Contrasting eastern-Pacific and central-Pacific types of ENSO. *J. Climate*, **22**, 615–632, https://doi.org/10.1175/2008JCLI2309.1.

Kashino, Y., N. Espana, F. Syamsudin, K. J. Richards, T. Jensen, P. Dutrieux, and A. Ishida, 2009: Observations of the North Equatorial Current, Mindanao Current, and Kuroshio current system during the 2006/07 El Niño and 2007/08 La Niña. *J. Oceanogr.*, **65**, 325–333, https://doi.org/10.1007/s10872-009-0030-z.

——, A. Ishida, and S. Hosoda, 2011: Observed ocean variability in the Mindanao Dome region. *J. Phys. Oceanogr.*, **41**, 287–302, https://doi.org/10.1175/2010JPO4329.1.

——, A. Atmadipoera, Y. Kuroda, and Y. Lukijanto, 2013: Observed features of the Halmahera and Mindanao Eddies. *J. Geophys. Res. Oceans*, **118**, 6543–6560, https://doi.org/10.1002/2013JC009207.

Kessler, W. S., 2006: The circulation of the eastern tropical Pacific: A review. *Prog. Oceanogr.*, **69**, 181–217, https://doi.org/10.1016/j.pocean.2006.03.009.

——, and B. A. Taft, 1987: Dynamic heights and zonal geostrophic transports in the central tropical Pacific during 1979–84. *J. Phys. Oceanogr.*, **17**, 97–122, https://doi.org/10.1175/1520-0485(1987)017<0097:DHAZGT>2.0.CO;2.

——, G. C. Johnson, and D. W. Moore, 2003: Sverdrup and nonlinear dynamics of the Pacific Equatorial Currents. *J. Phys. Oceanogr.*, **33**, 994–1008, https://doi.org/10.1175/1520-0485(2003)033<0994:SANDOT>2.0.CO;2.

Levine, A. F. Z., and M. J. McPhaden, 2016: How July 2014 easterly wind burst gave the 2015–2016 El Niño a head start. *Geophys. Res. Lett.*, **43**, 6503–6510, https://doi.org/10.1002/2016GL069204.

Li, Y., F. Wang, and F. Zhai, 2012: Interannual variations of subsurface spiciness in the Philippine Sea: Observations and mechanism. *J. Phys. Oceanogr.*, **42**, 1022–1038, https://doi.org/10.1175/JPO-D-12-06.1.

Liu, H., H. Zhou, W. Yang, X. Liu, Y. Li, Y. Yang, X. Chen, and X. Li, 2021: A three-dimensional gravest empirical mode determined from hydrographic observations in the western equatorial Pacific Ocean. *J. Mar. Syst.*, **214**, 103487, https://doi.org/10.1016/j.jmarsys.2020.103487.

Liu, X., and H. Zhou, 2020: Seasonal variations of the North Equatorial Current across the Pacific Ocean. *J. Geophys. Res. Oceans*, **125**, e2019JC015895, https://doi.org/10.1029/2019JC015895.

Masumoto, Y., and T. Yamagata, 1991: Response of the western tropical Pacific to the Asian winter monsoon: The generation of the Mindanao Dome. *J. Phys. Oceanogr.*, **21**, 1386–1398, https://doi.org/10.1175/1520-0485(1991)021<1386:ROTWTP>2.0.CO;2.

Masunaga, H., and T. S. L'Ecuyer, 2011: Equatorial asymmetry of the east Pacific ITCZ: Observational constraints on the underlying processes. *J. Climate*, **24**, 1784–1800, https://doi.org/10.1175/2010JCLI3854.1.

Meyers, G., and J. R. Donguy, 1984: The North Equatorial Countercurrent and heat storage in the western Pacific Ocean during 1982–83. *Nature*, **312**, 258–260, https://doi.org/10.1038/312258a0.

Nitani, H., 1972: Beginning of the Kuroshio. *Kuroshio: Physical Aspect of the Japan Current*, H. Stommel and K. Yoshida, Eds., University of Washington Press, 129–164.

Paek, H., J.-Y. Yu, and C. Qian, 2017: Why were the 2015/2016 and 1997/1998 extreme El Niños different? *Geophys. Res. Lett.*, **44**, 1848–1856, https://doi.org/10.1002/2016GL071515.

Pedlosky, J., 1987: *Geophysical Fluid Dynamics*. 2nd ed. Springer-Verlag, 710 pp.

Philander, S. G. H., W. J. Hurlin, and A. D. Seigel, 1987: Simulation of the seasonal cycle of the tropical Pacific Ocean. *J. Phys. Oceanogr.*, **17**, 1986–2002, https://doi.org/10.1175/1520-0485(1987)017<1986:SOTSCO>2.0.CO;2.

Phillips, N. A., 1951: A simple three-dimensional model for the study of large-scale extratropical flow patterns. *J. Meteor.*, **8**, 381–394, https://doi.org/10.1175/1520-0469(1951)008<0381:ASTDMF>2.0.CO;2.

Picaut, J., and T. Delcroix, 1995: Equatorial wave sequence associated with warm pool displacements during the 1986–1989 El Niño–La Niña. *J. Geophys. Res.*, **100**, 18 393–18 408, https://doi.org/10.1029/95JC01358.

Qiu, B., 1999: Seasonal eddy field modulation of the North Pacific subtropical countercurrent: TOPEX/Poseidon observations and theory. *J. Phys. Oceanogr.*, **29**, 2471–2486, https://doi.org/10.1175/1520-0485(1999)029<2471:SEFMOT>2.0.CO;2.

——, 2000: Interannual variability of the Kuroshio Extension system and its impact on the wintertime SST field. *J. Phys. Oceanogr.*, **30**, 1486–1502, https://doi.org/10.1175/1520-0485(2000)030<1486:IVOTKE>2.0.CO;2.

——, and T. M. Joyce, 1992: Interannual variability in the mid- and low-latitude western North Pacific. *J. Phys. Oceanogr.*, **22**, 1062–1079, https://doi.org/10.1175/1520-0485(1992)022<1062:IVITMA>2.0.CO;2.

——, and R. Lukas, 1996: Seasonal and interannual variability of the North Equatorial Current, the Mindanao Current, and the Kuroshio along the Pacific western boundary. *J. Geophys. Res.*, **101**, 12 315–12 330, https://doi.org/10.1029/95JC03204.

——, and S. M. Chen, 2004: Seasonal modulations in the eddy field of the South Pacific Ocean. *J. Phys. Oceanogr.*, **34**, 1515–1527, https://doi.org/10.1175/1520-0485(2004)034<1515:SMITEF>2.0.CO;2.

——, and S. Chen, 2012: Multidecadal sea level and gyre circulation variability in the northwestern tropical Pacific Ocean. *J. Phys. Oceanogr.*, **42**, 193–206, https://doi.org/10.1175/JPO-D-11-061.1.

——, ——, and H. Sasaki, 2013: Generation of the North Equatorial Undercurrent jets by triad baroclinic Rossby wave interactions. *J. Phys. Oceanogr.*, **43**, 2682–2698, https://doi.org/10.1175/JPO-D-13-099.1.

——, ——, B. S. Powell, P. L. Colin, D. L. Rudnick, and M. C. Schönau, 2019: Nonlinear short-term upper ocean circulation

variability in the tropical western Pacific. *Oceanography*, **32**, 22–31, https://doi.org/10.5670/oceanog.2019.408.

Qu, T., and R. Lukas, 2003: The bifurcation of the North Equatorial Current in the Pacific. *J. Phys. Oceanogr.*, **33**, 5–18, https://doi.org/10.1175/1520-0485(2003)033<0005:TBOTNE>2.0.CO;2.

Ren, H.-L., and F.-F. Jin, 2011: Niño indices for two types of ENSO. *Geophys. Res. Lett.*, **38**, L04704, https://doi.org/10.1029/2010GL046031.

Richards, K. J., S.-P. Xie, and T. Miyama, 2009: Vertical mixing in the ocean and its impact on the coupled ocean–atmosphere system in the eastern tropical Pacific. *J. Climate*, **22**, 3703–3719, https://doi.org/10.1175/2009JCLI2702.1.

Roemmich, D., and J. Gilson, 2001: Eddy transport of heat and thermocline waters in the North Pacific: A key to interannual/decadal climate variability? *J. Phys. Oceanogr.*, **31**, 675–687, https://doi.org/10.1175/1520-0485(2001)031<0675:ETOHAT>2.0.CO;2.

——, and ——, 2009: The 2004–2008 mean and annual cycle of temperature, salinity, and steric height in the global ocean from the Argo Program. *Prog. Oceanogr.*, **82**, 81–100, https://water.doi.org/10.1016/j.pocean.2009.03.004.

Schott, G., 1939: Die äquatorialen Strömungen des westlichen Stillen Ozeans. *Ann. Hydrogr. Berl.*, **67**, 247–257.

Song, L. N., Y. Li, J. Wang, F. Wang, S. Hu, C. Liu, X. Diao, and C. Guan, 2018: Tropical meridional overturning circulation observed by subsurface moorings in the western Pacific. *Sci. Rep.*, **8**, 7632, https://doi.org/10.1038/s41598-018-26047-7.

Spall, M. A., 1996: Dynamics of the Gulf Stream/deep western boundary current crossover. Part II: Low-frequency internal oscillations. *J. Phys. Oceanogr.*, **26**, 2169–2182, https://doi.org/10.1175/1520-0485(1996)026<2169:DOTGSW>2.0.CO;2.

Sprintall, J., S. Kennan, Y. Y. Kim, and P. Niiler, 2009: Wind-driven ageostrophic transport in the North Equatorial Countercurrent of the eastern Pacific at 95°W. *J. Phys. Oceanogr.*, **39**, 2985–2998, https://doi.org/10.1175/2009JPO4088.1.

Suarez, M. J., and P. S. Schopf, 1988: A delayed action oscillator for ENSO. *J. Atmos. Sci.*, **45**, 3283–3287, https://doi.org/10.1175/1520-0469(1988)045<3283:ADAOFE>2.0.CO;2.

Taft, B. A., and W. S. Kessler, 1991: Variations of zonal currents in the central tropical Pacific during 1970 to 1987: Sea level and dynamic height measurements. *J. Geophys. Res.*, **96**, 12 599–12 618, https://doi.org/10.1029/91JC00781.

Tan, S., and H. Zhou, 2018: The observed impacts of the two types of El Nino on the North Equatorial Countercurrent in the Pacific Ocean. *Geophys. Res. Lett.*, **45**, 10 493–10 500, https://doi.org/10.1029/2018GL079273.

Toole, J. M., R. C. Millard, Z. Wang, and S. Pu, 1990: Observations of the Pacific North Equatorial Current

bifurcation at the Philippine coast. *J. Phys. Oceanogr.*, **20**, 307–318, https://doi.org/10.1175/1520-0485(1990)020<0307:OOTPNE>2.0.CO;2.

Tozuka, T., T. Kagimoto, Y. Masumoto, and T. Yamagata, 2002: Simulated multiscale variations in the western tropical Pacific: The Mindanao Dome revisited. *J. Phys. Oceanogr.*, **32**, 1338–1359, https://doi.org/10.1175/1520-0485(2002)032<1338:SMVITW>2.0.CO;2.

Wang, C. Z., R. H. Weisberg, and J. I. Virmani, 1999: Western Pacific interannual variability associated with the El Niño-Southern Oscillation. *J. Geophys. Res.*, **104**, 5131–5149, https://doi.org/10.1029/1998JC900090.

Wang, F., J. N. Wang, C. Guan, Q. Ma, and D. X. Zhang, 2016: Mooring observations of equatorial currents in the upper 1000 m of the western Pacific Ocean during 2014. *J. Geophys. Res. Oceans*, **121**, 3730–3740, https://doi.org/10.1002/2015JC011510.

Weisberg, R. H., and C. Z. Wang, 1997: A western Pacific oscillator paradigm for the El Niño–Southern Oscillation. *Geophys. Res. Lett.*, **24**, 779–782, https://doi.org/10.1029/97GL00689.

Wyrtki, K., 1961: Physical oceanography of the Southeast Asian water. Scientific Results of Marine Investigation of the South China Sea and Gulf of Thailand, 1959-1961, NAGA Rep. Vol. 2, 195 pp.

——, 1975: El Niño—The dynamic response of equatorial Pacific Ocean to atmospheric forcing. *J. Phys. Oceanogr.*, **5**, 572–584, https://doi.org/10.1175/1520-0485(1975)005<0572:ENTDRO>2.0.CO;2.

——, 1979: Response of sea surface topography to the 1976 El Niño. *J. Phys. Oceanogr.*, **9**, 1223–1231, https://doi.org/10.1175/1520-0485(1979)009<1223:TROSST>2.0.CO;2.

——, 1985: Water displacements in the Pacific and the genesis of El Niño cycles. *J. Geophys. Res.*, **90**, 7129–7132, https://doi.org/10.1029/JC090iC04p07129.

——, and R. Kendall, 1967: Transports of Pacific equatorial countercurrent. *J. Geophys. Res.*, **72**, 2073–2076, https://doi.org/10.1029/JZ072i008p02073.

Yuan, D., Z. Zhang, P. C. Chu, and W. K. Dewar, 2014: Geostrophic circulation in the tropical North Pacific Ocean based on Argo profiles. *J. Phys. Oceanogr.*, **44**, 558–575, https://doi.org/10.1175/JPO-D-12-0230.1.

Zhao, J., Y. L. Li, and F. Wang, 2013: Dynamical responses of the west Pacific North Equatorial Countercurrent (NECC) system to El Niño events. *J. Geophys. Res. Oceans*, **118**, 2828–2844, https://doi.org/10.1002/jgrc.20196.

Zhou, H., D. Yuan, R. Li, and L. He, 2010: The western South China Sea currents from measurements by Argo profiling floats during October to December 2007. *Chin. J. Oceanol. Limnol.*, **28**, 398–406, https://doi.org/10.1007/s00343-010-9052-z.